BBA - Bioenergetics 1861 (2020) 148091

Contents lists available at ScienceDirect

BBA - Bioenergetics

journal homepage: www.elsevier.com/locate/bbabio

# The spatio-temporal organization of mitochondrial $F_1F_O$ ATP synthase in cristae depends on its activity mode

Kirill Salewskij[a,1], Bettina Rieger[a,1], Frances Hager[a], Tasnim Arroum[a], Patrick Duwe[a], Jimmy Villalta[a], Sara Colgiati[b,c], Christian P. Richter[d,e], Olympia E. Psathaki[d,e], José A. Enriquez[b], Timo Dellmann[a], Karin B. Busch[a,*]

[a] University Münster, Department of Biology, Institute of Molecular Cell Biology, 48149 Münster, North Rhine-Westphalia, Germany
[b] Centro Nacional de Investigaciones Cardiovasculares Carlos III, 28029 Madrid, Catania, Spain
[c] Institute of Nutrition and Food Technology, Biomedical Research Centre, Department of Physiology, University of Granada, Granada, Andalusia, Spain
[d] University of Osnabrück, School of Biology, University of Osnabrück, 49076 Osnabrück, Lower Saxony, Germany
[e] Center of Cellular Nanoanalytics, Integrated Bioimaging Facility, University of Osnabrück, 49076 Osnabrück, Lower Saxony, Germany

ARTICLE INFO

*Keywords:*
$F_1F_O$ ATP synthase
Mitochondria
Spatio-temporal organization
Superresolution microscopy
Tracking and localization microscopy (TALM)
Ultrastructure
OXPHOS
Reverse ATP synthase activity
ATP synthase dimers
Metabolic adaptation

ABSTRACT

$F_1F_O$ ATP synthase, also known as complex V, is a key enzyme of mitochondrial energy metabolism that can synthesize and hydrolyze ATP. It is not known whether the ATP synthase and ATPase function are correlated with a different spatio-temporal organisation of the enzyme. In order to analyze this, we tracked and localized single ATP synthase molecules *in situ* using live cell microscopy. Under normal conditions, complex V was mainly restricted to cristae indicated by orthogonal trajectories along the cristae membranes. In addition confined trajectories that are quasi immobile exist. By inhibiting glycolysis with 2-DG, the activity and mobility of complex V was altered. The distinct cristae-related orthogonal trajectories of complex V were obliterated. Moreover, a mobile subpopulation of complex V was found in the inner boundary membrane. The observed changes in the ratio of dimeric/monomeric complex V, respectively less mobile/more mobile complex V and its activity changes were reversible. In IF1-KO cells, in which ATP hydrolysis is not inhibited by IF1, complex V was more mobile, while inhibition of ATP hydrolysis by BMS-199264 reduced the mobility of complex V. Taken together, these data support the existence of different subpopulations of complex V, ATP synthase and ATP hydrolase, the latter with higher mobility and probably not prevailing at the cristae edges. Obviously, complex V reacts quickly and reversibly to metabolic conditions, not only by functional, but also by spatial and structural reorganization.

## 1. Introduction

In respiring cells, ATP is mainly provided by oxidative phosphorylation (OXPHOS) involving five membrane protein complexes (CI-CV) in the inner mitochondrial membrane. Their joined task is to oxidize $NADH/H^+$ (complex I) and $FADH_2$ (complex II) to generate a proton motive force across the inner membrane (complexes I, III, IV) and to synthesize ATP ($F_1F_O$ ATP synthase, complex V). Tumor cells, often used in research, usually have a reduced oxidative metabolism and switch to glycolytic energy metabolism – a phenomenon known as the Warburg effect [1,2]. By changing the sugar supply, this can be reversed [3]. Morphology and internal architecture of mitochondria are responsive to mitochondrial function [4–7]. The mitochondrial ultrastructure is modulated by several inner membrane proteins, including the Optic atrophy 1 protein OPA1 [8], compounds of the MICOS complex at the cristae junctions [9–11], and $F_1F_O$ ATP synthase [12]. Moreover, new studies suggest that these main players are functionally coupled, e.g. high OPA1 levels [13] and Mic10/Mic27 [14] apparently stabilize complex V oligomerization. Habitually, $F_1F_O$ ATP synthase assembles into rows of dimers at the small rims of lamellar or tubular

*Abbreviations:* 2-DG, 2-Deoxy-D-glucose; CM, cristae membranes; EMCCD, electron multiplying charge-coupled device; HK, hexokinase; IBM, inner boundary membrane; ICS, intracristal space; IMM, inner mitochondrial membrane; MSD, mean square displacement; OMM, outer mitochondrial membrane; OXPHOS, oxidative phosphorylation; SU, subunit; TALM, tracking and localization microscopy

* Corresponding author at: Institute of Molecular Cellbiology, Schloßplatz 5, 48149 Münster, Germany.
*E-mail address:* buschkar@uni-muenster.de (K.B. Busch).

[1] Authors contributed equally.

https://doi.org/10.1016/j.bbabio.2019.148091
Received 31 May 2019; Received in revised form 2 October 2019; Accepted 18 October 2019
Available online 27 November 2019

cristae [15,16]. Analysis of distances between complex V by 3D-STORM superresolution suggests that stress conditions affecting respiration also alter complex V dimer organization [17,18]. These observations imply that complex V exhibits specific spatio-temporal dynamics which allows such re-organization. Indeed, single particle tracking and FRAP studies have shown that the complex V is in principal diffusive in the inner membrane [19–21], which suggest that the assembly of complex V into rows of dimers is reversible.

The purpose of this study was to monitor the underlying dynamics of ATP synthase/ATPase organization in response to metabolic switches. We monitored the spatio-temporal organization of complex V with a particular focus on its mobility in the inner membrane. To induce a short-term metabolic switch, the enzyme Hexokinase, which has a key function at the junction between glycolysis and respiration, was inhibited by the non-fermentable sugar 2-Deoxy-D-glucose (2-DG) [22,23]. This resulted in an intermediate depletion of substrate for the respiratory chain, measurable by a decrease in extracellular acidification rate as well as maximal and spare oxygen consumption rate. However, it seems that this decrease did not result in decreased ATP synthesis in mitochondria. On contrary, we found an increased mitochondrial ATP production rate – correlating with a lower mitochondrial membrane potential $\Delta\Psi_m$. As inhibitor studies suggested, ATP hydrolysis - in addition to ATP synthesis - apparently took place before 2-DG treatment. To dissect whether ATPase Inhibitory Factor 1 (IF1) and spatial separation of ATP synthesis and hydrolysis might be a clue, we determined the localization and mobility of complex V molecules under different conditions. Therefore, we fluorescence-labeled complex V and recorded its localization and dynamics on the single molecule level by means of Tracking and Localization Microscopy (TALM) [19,24]. Trajectories of $F_1F_O$ ATP synthase particles were obtained from single particle tracking experiments with the Multiple-Target Tracing Algorithm (MTT) [25]. We found that increased ATP synthesis in 2-DG treated cells was accompanied by a slight decrease of the dimer/monomer ratio and a narrowing of cristae. In addition, the complex V showed a different localization pattern in cristae, with decreased diffusion coefficients. When ATP synthesis decreased again, complex V reorganized and showed the same localization and mobility pattern as before. Furthermore, cristae widened again. Moreover, complex V diffusion was decreased upon chemically inhibition of ATP hydrolysis, but increased under conditions where the factor for physiological inhibition of ATP hydrolysis was knocked out. Thus, our data show that spatio-temporal organization of complex V is determined by the specific metabolic setting, which here was given as a reversible inhibition of glycolysis.

## 2. Materials and methods

### 2.1. Cell culture and labeling

Stable transfected HeLa cells expressing SU γ-HaloTag® were cultivated in Minimal Essential Medium Earle's Salt (5.6 mM glucose + L-glutamine) supplemented with 10% FBS (Fetal bovine serum), 1% HEPES and 1% NEAA (non-essential amino acids) at 37 °C and 5% $CO_2$. When confluence was reached, cells were split using 1 mL Trypsin/EDTA for 5 min at 37 °C (and 5% $CO_2$). Labeling and preparation of single molecule studies is described in detail elsewhere [19,24].

### 2.2. Metabolic studies

Oxygen consumption rates (OCR) and extracellular acidification rates (ECAR) of intact HeLa cells were recorded with the Seahorse $XF^e96$ Extracellular Flux Analyzer (Agilent Technologies). 25.000 cells were seeded per well of a 96-well XF cell culture microplate 24 h before the experiment. Before loading into the $XF^e$ Analyzer, control cells were washed with XF base medium adjusted to pH 7.4 (Minimal DMEM, 0 mM Glucose, 102353-100 from Agilent), placed in fresh XF base medium pH 7.4 with supplements (1 mM pyruvate, 2 mM L-glutamine, and 5.6 mM D-glucose) and shortly incubated at 37 °C. Supplements were from Carl Roth GmbH + Co. KG. To inhibit glycolysis, 30 mM 2-Deoxy-D-glucose (2-DG, Sigma Aldrich) was added to the 5.6 mM glucose MEM and XF base media with supplements. After recording resting respiration in the analyzer, a mitochondrial stress test was performed. Therefore, the following chemicals from Seahorse Biosciences were added sequentially to the cells: oligomycin (1 μM) to inhibit the ATP synthase; trifluoromethoxy carbonylcyanide phenylhydrazone (FCCP, 0.5 μM) an uncoupler of respiration and ATP synthesis, and inhibitors for complex I (rotenone; 0.5 μM) and complex III (antimycin A; 0.5 μM). In each experiment, three time points with a 6 min interval were recorded for the basal oxygen consumption rate (OCR). In a second experiment analyzing mitochondrial fuel usage, the following chemicals from Agilent (former Seahorse Biosciences) were added sequentially to the cells: UK5099 (2-Cyano-3-(1-phenyl-1H-indol-3-yl)-2-propenoic acid, 2 μM), to inhibit the glucose oxidation pathway by blocking the mitochondrial pyruvate carrier (MPC); BPTES (Bis-2-(5-phenylacetamido-1,3,4-thiadiazol-2-yl) ethyl sulfide, 3 μM), an allosteric inhibitor of glutaminase (GLS1), to inhibit the glutamine oxidation pathway; Etomoxir (4 μM), to inhibit long chain fatty acid oxidation by blocking the carnitine palmitoyl-transferase 1A (CPT1A). By subsequent addition of the inhibitors of metabolic pathways (glucose, GLC; glutamine, GLU and fatty acid, FA catabolism), fuel dependency was determined. Three measurements were conducted for the resting OCR, five after the first injection and five after the second injection with a 2-min interval of recording followed by 2 min of mixing and 2 min of incubation for each measurement. In a third experiment referred to as ATP rate assay, XF base medium pH 7.4 with additional supplementation of 5 mM HEPES was used. The assays to dissect mitochondrial from glycolytic ATP synthesis rates follows suggestions made by Mookerjee and co-workers [41]. Injections: Oligomycin (1.5 μM) to inhibit the ATP synthase; inhibitors for complex I (rotenone; 0.5 μM) and complex III (antimycin A; 0.5 μM). Inhibitors were purchased from Agilent (Agilent Seahorse XF Real-Time ATP Rate Assay Kit 103592-100). Agilent Seahorse XF technology measures the flux of both $H^+$ production (ECAR) and $O_2$ consumption (OCR), simultaneously. By obtaining OCR and ECAR data under basal conditions and after serial addition of mitochondrial inhibitors (oligomycin and rotenone/antimycin A), total cellular ATP Production Rates and pathway-specific mitoATP and glycoATP Production Rates can be measured. The series of calculations used to transform the OCR and ECAR data to ATP Production Rates is performed using the Agilent Seahorse XF Real-Time ATP Rate Assay Report Generator, described in the according user guide. Briefly: Glycolytic ATP Production Rate (pmol ATP/min) = glycoPER (pmol $H^+$/min) is associated with the conversion of glucose to lactate in the glycolytic pathway; Mitochondrial ATP production rate: $OCR_{ATP}$ (pmol $O_2$/min) = OCR (pmol $O_2$/min) - $OCR_{Oligo}$ (pmol $O_2$/min) is associated with oxidative phosphorylation in the mitochondria. Total ATP production rate: Glycolytic ATP Production Rate + Mitochondrial ATP Production Rate. Cell counting: Cell number per well was measured after ATP rate assay performance by counting fluorescently labeled nuclei from images captured by Cytation 1 (BioTek). Therefore, cells were stained with 2 μg/mL Hoechst 33342 (Sigma) and the nuclear images were captured using a 4× lens with a DAPI filter. Cells (the individual nuclei) were counted by BioTek Cytation 1 using the XF Cell Imaging and Counting software2 and data was normalized in Wave software.

### 2.3. Generation of IF1-KO cell lines

The IF1-knockout cells were manufactured using the CRISPR/Cas technique. The first step was to find the appropriate targeting sequence for crRNA in the vicinity of the START codon. The crRNA was cloned into the pSpCas9(BB)-2A-GFP (PX458) vector (Addgene). Thus, the resulting vector contained both sgRNA and Cas9 nuclease. To enable

selection with Puromycin, the *pac* gene was inserted at the cutting site. For this purpose, a construct was cloned with homologous arms to the right and left of the place where Cas9 is to be cut with the *pac*-gen in between. HeLa cells were cotransfected with both constructs and transformed cells were selected by Puromycin treatment. Positive clones were isolated and the IF1 knockdown tested by qPCR.

### 2.4. ROS measurements

Before staining, culture medium was exchanged to PBS (phosphate buffered saline w/o $Ca^{2+}$ and $Mg^{2+}$) plus 1% FBS (fetal bovine serum). For ROS detection, cells were stained with 2.5 nM of CellROX™ Deep Red ($\lambda_{ex/em}$~644/665 nm) in PBS for 30 min. After washing twice with PBS, flow cytometry analysis was performed with the adequate laser and band pass filter (exc. 660/10 nm, em. 690/50 nm). For the time course of ROS levels in dependency on 2-DG application, microscopic analysis was conducted (cLSM, 63× objective). HeLa cells that stable expressed a matrix-targeted GFP were stained with the ROS sensitive dye MitoTracker®CM-H2XRos Red (200 nm for 30 min) and then washed twice with PBS. MitoTracker Red CM-H2XRos is a reduced, non-fluorescent version of MitoTracker Red (M-7512, Thermofisher) that fluoresces upon oxidation. The emission of MitoTracker Red CM-H2XRos was set to 600–700 nm (exc. 579 nm). For imaging, medium without phenol red was used. Before 2-DG application (30 mM), cells were imaged ($t$ = 0 min). Every 5 min, several images were taken at different positions to minimize photobleaching effects. N = 3 technical replicates. The fluorescence intensities were analyzed with ImageJ (MacBiophotonics). The ROS signal was normalized to the mt-GFP signal.

### 2.5. Measurement of mitochondrial membrane potential

Mitochondrial membrane potential $\Delta\Psi_m$ was measured using the $\Delta\Psi_m$ sensitive dye tetramethylrhodamine ethyl ester (TMRE, 7 nM) [26]. The dye was excited at 561 nm, and the emission recorded between 600 and 700 nm at a fluorescence microscope. For normalization on the mitochondrial mass, mitochondria in addition were stained with MitoTracker™ Green (MTG, 100 nM). The fluorescence of MTG is supposed to be membrane potential independent [27]. MTG was excited at 488 nm, emission was recorded between 510 and 540 nm. *Z*-stacks of 7 slices (step size of 360 nm) were recorded. The fluorescence intensity was analyzed with ImageJ (MacBiophotonics). The ratio of the TMRE/MTG signal indicates the relative value of the $\Delta\Psi_m$.

### 2.6. Fluorescence microscopy

Fluorescence imaging was carried out with confocal laser scanning microscope (Leica TCS SP8 SMD) equipped with a 63× water objective (N.A. 1.2) and a tunable white light laser. HyD's with GaASP photocathodes were used as detectors. Measurements were performed at 37 °C and 5% $CO_2$. For determination of fluorescence intensities of fluorescent dyes specifically accumulating in mitochondrial compartments, mean grey values of the whole mitochondrial network are measured after automatic clustering-based image thresholding by application of the Otsu's thresholding in the open source Fiji program.

### 2.7. ATP determination

Relative ATP was determined by using a FRET sensor composed of the ε-subunit of complex V from *Bacillus spec*. sandwiched between Clover and mRuby2 (Clover-ATeam-mRuby2), modified from the original ATeam [28]. FRET was determined via fluorescence lifetime (τ) decrease of the donor with increasing ATP. τ was determined in the time domain with a time correlated single photon counting device (Piqoquant/Leica) docked to the cLSM. Clover was excited at 488 nm with a pulsed white light laser (40 MHz), emission was recorded from 520 to 560 nm using a BS560, Bandpass filter I BP500-550. For the decay histograms, at least 1000 photons were collected per pixel.

### 2.8. Single molecule tracking and localization microscopy

Single molecule tracking and localization was performed at a room temperature with an inverted microscope (Nikon, Eclipse TE2000) equipped with a TIRF condenser, an oil immersion objective designed for TIRF (100× oil/N.A. 1.49/0.12 Apochromat, Nikon), an EMCCD camera (Evolve™512, Photometrics, 512 × 512 pixel imaging array, 16 μm × 16 μm pixel area). To fulfil the Nyquist-oversampling, a 1.5x magnitude focussing lens was used. A quad line beam splitter (zt405/488/561/633–640) was mounted in combination with an emission quadband filter (HC 446 nm/523 nm/600 nm/677 nm). A 561 nm laser (Melles Griot, 20 mW, DPSS) was coupled into the device via a single-mode glass fiber (FC/PC). The measurements were performed as described before [29]. In short, HeLa cells stable transfected with $F_1F_O$ ATP synthase subunit ɣ fused C-terminally to a HaloTag were post-translationally labeled with $TMR^{HTL}$ (1 nM) for 20 min, washed twice in PBS and once in medium without phenol red before imaging. Assembly and correct intramitochondrial localization were shown earlier with constructs where similar sized EGFP and pHluorin, respectively, were genetically fused to the same position in SU γ as exchange of by the HaloTag7 [30,31]. The $TMR^{HTL}$ concentration was set for sub-stoichiometric labeling and low enough to visualize single molecule signals. The incident angle was set to achieve a highly inclined laminated optical light sheet [32]. Usually, 3000 frames were recorded. Frame rates were 33 Hz and 50 Hz, respectively. Individual signals with a signal to noise ratio above 5 were fitted with a 2D Gaussian fit for localizing molecules. From all frames, a cumulative localization map was generated after movement of mitochondria during the recording time was excluded. For generating trajectory maps, single molecules in subsequent frames were connected when the following criteria were matched: they must have been within a radius of maximal 2 px (pixel size 107 nm) and the intensity distribution profile must have been identical. Only trajectories with a minimum duration of 160 ms were analyzed.

### 2.9. Theoretical background

Single fluorescent molecules, whose size is below the diffraction limit, project a three-dimensional diffraction pattern onto the image plane, which is defined as the point spread function (PSF). The PSF can be calculated by Abbe's law and used to localize single emitters by a 2D Gaussian fit [33–35]:

$$d = \frac{\lambda}{2NA} = \frac{\lambda}{2n * \sin(\theta)} \quad (1)$$

with $d$ being the diameter of the PSF, λ as the wavelength of the emitted light and $NA$ being the numerical aperture of the microscope's objective. The numerical aperture describes the light gathering capability of an objective and depends on the refractive index $n$ of the medium in which the lens is used and the half angular aperture of the objective θ. The "full width at half maximum" (FWHM) criterion is used to describe a PSF, whereby FWHM is the width at 50% of the intensity maximum. For TMR ($\lambda_{em.}$ = 582 nm) and an objective with NA of 1.49, the PSF diameter is approximately 390 nm.

According to the Rayleigh criterion, the resolution of the system is:

$$r = \frac{1.22\lambda}{2NA} = \frac{0{,}61\lambda}{n * \sin(\theta)} \quad (2)$$

where $r$ is the minimal distance between the two objects. $n$ is the refractive index of the medium between the objective and sample, λ is the wavelength of the emitted light, θ is the half angular aperture of the objective and $NA$ is the numerical aperture of the microscope objective. Practically, this means that two separate light points can just be

distinguished if the intensity maximum of the first point coincides with the first intensity minimum of the second point. Here, the theoretical resolution is ~240 nm. The pixel size was 106.7 nm for an EMCCD camera (512 × 512 px chip) with a pixel area of 16 µm × 16 µm, thus fulfilling the Nyquist-Shannon sampling theorem which demands a 2fold oversampling rate for the desired spatial resolution. In order to probe the spatio-temporal behavior of $F_1F_O$ ATP synthase, the multi-target tracer was used [25]. The first step of single-particle tracking (SPT) involves the localization of the particle by a 2D Gaussian fit. The accuracy of this localization highly depends on the occurrence of discrete signals, the pixel size of the EMCCD/CMOS camera and the photon emission of the molecule as well as the background noise:

$$\sigma_{\mu i} = \sqrt{\left(\frac{s_i^2}{N}\right) + \left(\frac{a^2/12}{N}\right) + \left(\frac{8\pi s_i^4 b^2}{a^2 N^2}\right)} \quad (3)$$

where σ is the standard error of the mean value of photon distribution, $N$ is the number of gathered photons, $a$ is the pixel size of the EMCCD/CMOS detector, $b$ is the standard deviation of the background and $s_i$ is the standard deviation in dimension $i$, with $i$ being either $x$ or $y$ dimension.

### 2.10. Single molecule localization and tracking

Single molecules are recorded over several frames and then are localized by a 2D Gaussian mask. The multiple-target tracing algorithm (MTT) [25] is used to generate trajectories. To obtain diffusion data, the mean square displacement is determined (MSD) and the diffusion coefficient is calculated according to:

$$r^2 = 2n4D\Delta t^{\alpha} + 4\varepsilon^2 \quad (4)$$

$$D = \frac{r^2 - 4\varepsilon^2}{2n4\Delta t^{\alpha}}, \quad (5)$$

where $r^2$ is the MSD, $D$ is the lateral diffusion coefficient, $\Delta t$ is the lag time, $n$ is the dimension and ε is the localization error. The exponent α is a factor that distinguishes modes of diffusion, with $\alpha < 1$ for anomalous diffusion. Anomalous diffusion is expected when the movement of particles is restricted by structural constraints such as physical obstacles or inclusion in micro-compartments. Further details are found in Appelhans et al. [29].

### 2.11. Transmission electron microscopy

For transmission electron microscopy (TEM) HeLa cells from the different conditions were fixed for 2 h at room temperature (RT) in 2.5% glutaraldehyde (Sciences Services, Germany) and in 0.1 M cacodylate buffer pH 7.4 (Sciences Services, Germany), subsequently washed in 0.1 M cacodylate buffer pH 7.4, post-fixed for 2 h at RT in 1% osmium tetroxide/0.8% potassium ferrocyanide in 0.1 M cacodylate buffer pH 7.4, dehydrated stepwise in a graded ethanol series and embedded in Epon 812 (Fluka, Buchs, Switzerland). Ultrathin sections (70 nm, ultramicrotome EM UC7, Leica, Wetzlar, Germany) were afterwards stained for 30 min with 1% uranyl acetate (Leica, Germany) and 20 min in 3% lead citrate (Leica, Germany). TEM images were acquired with a 200 kV transmission electron microscope (JEM2100-Plus, Jeol Japan). The cristae width was determined as following: TEM images were inverted. Line plots were perpendicularly placed to the length of cristae (ImageJ™). The line plot intensity profiles showed two peaks corresponding to the intensity of the negative stained membranes. The distance between the peaks was taken as cristae width. Per crista, two to three line plots were drawn for the determination of the crista width.

### 2.12. Blue Native page electrophoresis assays

Mitochondria from the indicated cell lines were isolated as follows. HeLa cells were cultured in Minimum Essential Medium Eagle (MEM) supplemented with 10% fetal calf serum (FCS); 1% non-essential amino acids (NEAS), 1% HEPES, and 1% glutamine (MEM + +) in T175 flask and maintained in 37 °C with 5% $CO_2$ during the experiment. For starvation, the medium was aspired and exchanged to fresh MEM + + supplemented with 30 mM sterile 2-DG. For mitochondrial isolation we used the cell homogenizer (Isobiotec, Germany) combined with 1 mL Glas syringes (Hamilton, USA) as described in Schmitt et al. [36]. Cells were trypsinized and separated with syringe before homogenization. All steps were performed on ice, the Isolation buffer was freshly prepared, and all materials used were pre-cooled before each isolation. For HeLa cells, the 6 mm Tungsten carbide ball was used. Isolation buffer: 300 mM Sucrose, 5 mM TES, 200 µM EGTA, pH should be adjusted with KOH to 7.2. Protein concentration was determined via the Bradford method using BSA as a standard. 50 µg protein were loaded per pocket.

Mitochondria were further processed in the presence of Digitonin 6 g/g Mitochondria [37]. Dimers of ATP synthase were resolved by mean of high resolution Blue Native electrophoresis as described in Witting et al. 2007 [38]. After separation on a 3–13% gel, the proteins were electro-blotted onto Hybond-P-polyvinylidene fluoride (PVDF) membranes (GE Healthcare) and immune-blotted with a primary antibody against subunit β of ATP synthase (Abcam 14730, mouse monoclonal). The secondary antibody was anti-mouse dylight 800 from Rockland (610145002) and the signal detected using the Odyssey® Infrared Imaging System (Li-COR bioscience). The densito-metric analysis of the ratio between monomer and dimer of ATP synthase was performed using Gel Eval™ software.

### 2.13. Western blotting

Cells were washed twice in PBS and extracted in sample buffer. Depending on the confluency, 50 µL to 150 µL of SDS sample buffer was added to each well (0.83% SDS; 6.25 mM TRIS; 7.25% Glycerine; 0.0083% MercaptoEtOH; 0.01% Bromphenol blue) plus 0.1 µL Benzonase® nuclease was added to the reaction tubes. The solution was incubated at RT for 10 min. The extracted proteins were separated by SDS-PAGE and then transferred onto a polyvinylidene difluoride (PVDF) membranes by semi-dry blotting. Detection of OXPHOS complexes was done with a total rodent OXPHOS antibody cocktail (Abcam, Ab110413). Subunit β was detected with an anti-ATP5B antibody (proteintech #17247-1-AP), VDAC with an anti-VDAC antibody (Cell signalling #4661), subunit e with an anti-ATP5I antibody (abcam #122241). For the detection of bands, enhanced chemiluminescent substrate consisting of a 1:1 mix of Luminol/Enhancer & Peroxide solution was used.

### 2.14. Statistical analysis

Statistical analysis was performed using OriginPro version 9.6, 2019 (OriginLab Cooperation, Northhampton, MA). Student's $t$-test or ANOVA was used with subsequent post hoc test (Scheffé-Test) or pairwise comparisons if applicable (as indicated). For the calculation of the ratio dimer/monomer ($k = D / M$) the ratio $k$ was treated as a function of two variables $k$ ($D$, $M$). According to the error propagation law of Gauss, the partial derivative of each variable must first be formed from this function. Partial derivation to $D$ means, for example, that the function is differentiated to $D$ and $M$ is regarded as a constant. For the calculated value $k$, the error σ is obtained according to:

$$\sigma = \sqrt{\left(\frac{1}{M}\right)^2 * \sigma_D{}^2 + \left(-\frac{D}{M^2}\right)^2 * \sigma_M{}^2}$$

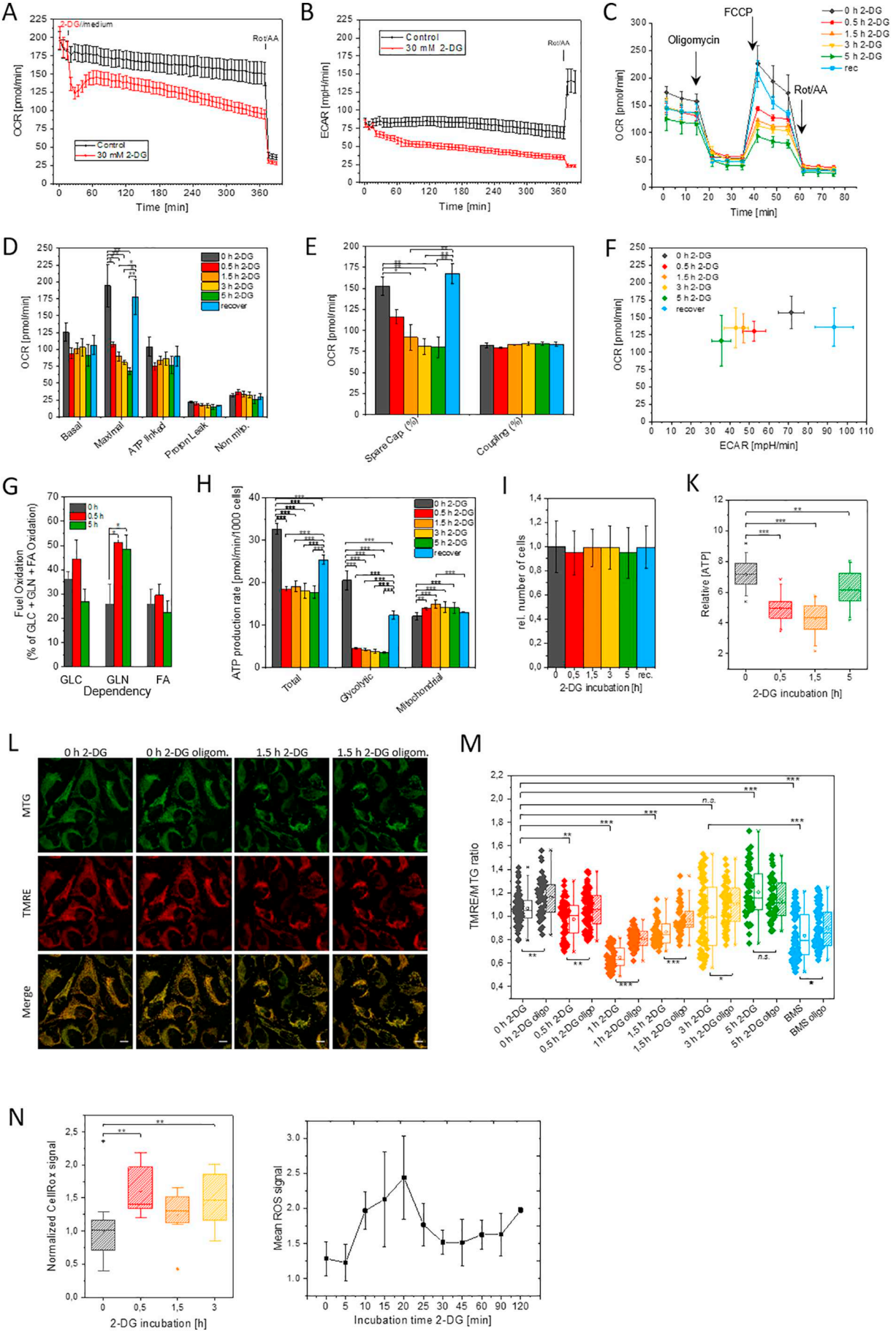


*(caption on next page)*

**Fig. 1.** Effect of glycolysis inhibition on mitochondrial respiration and physiology. (A–B) Mitochondrial oxygen consumption rates (OCR) and extracellular acidification rates (ECAR) when inhibiting glycolysis with 2-DG over an extended period of time ($N = 2$). (A) Effect of 2-DG-induced inhibition of glycolysis on oxygen consumption rate. After 6 h rotenone and antimycin A (Rot: 0.5 μM; AA: 0.5 μM) were added. (B) Parallel determination of ECAR under the same conditions. (C) OCR of HeLa cells under normal conditions (0 h, dark grey), 0.5 h (red) 1.5 h (orange), 3 h (yellow), 5 h (green) after 2-DG application and after recovery (= 3 h 2-DG followed by 2 h normal medium, blue) ($N = 3$ independent experiments). Time point 5 h is not shown here. After basal respiration monitoring, oligomycin (1 μM), uncoupler FCCP (trifluoromethoxy carbonylcyanide phenylhydrazone; 0.5 μM), rotenone and antimycin A (Rot, 0.5 μM; AA, 0.5 μM) were added at the indicated times to determine ATP linked respiration, maximum respiration and OXPHOS specific oxygen consumption, respectively. (D) OCR results for all time points including recovery conditions. Statistics were performed on means. (E) Spare capacity and coupling during 2-DG treatment (both in %). Statistics were performed on means. (F) Ratio of oxygen consumption (OCR) to extracellular acidification rate (ECAR) for metabolic phenotyping. (G) Fuel dependency change under 2-DG induced starvation. GLC: glucose, GLN: glutamine, FA: fatty acids ($N = 3$). 2-DG inhibition induces increased glutamine metabolism after 0.5 h. Statistics were performed on means; One Way ANOVA with post hoc Fisher LSD. (H) Dissection of glycolytic and mitochondrial ATP production rates. (I) 2-DG inhibition does not affect the cell number during the measurement time. Fluorescently labeled nuclei from images captured by Cytation 1 were counted. (K) Relative changes in cytosolic ATP levels determined by a modified ATeam, a FRET sensor for ATP [29] ($N = 2$). (L) Effect of 2-DG and oligomycin on mitochondrial membrane potential ($\Delta\Psi_m$), mass and morphology. TMRE (tetramethylrhodaminethyl ester, 7 nM) was used as $\Delta\Psi_m$ sensitive dye and MitoTracker™Green (MTG, 100 nM) as mitochondrial mass indicator [43]. (M) Effect of ATP synthase inhibition by oligomycin and ATPase inhibition by BMS-199264 during 2-DG treatment on $\Delta\Psi_m$. Oligomycin (1 μM), BMS (5 μM), 2-DG (30 mM), medium glucose (5.6 mM). Box and whisker plots: The boxes represent the 25th to 75th percentiles. The vertical lines in the boxes represent the median values, while the square symbols in the boxes represent the respective mean values. The minimum and maximum values are marked with x. Statistics: One Way ANOVA with post hoc Tukey test and Students *t*-test for pairwise comparison. $^{*}P \leq 0.05$; $^{**}P \leq 0.01$; $^{***}P \leq 0.001$. (N) For determination of mitochondrial ROS, cells stained with CellROX Deep Red were analyzed via flow cytometry analysis (left graph). Moreover, MitoTracker Red CM-H2XRos stained cells were analyzed with a fluorescence microscope (right graph). Statistics: One Way ANOVA with post hoc Tukey test (if not stated otherwise) performed on single values (if not stated otherwise). All measurements were performed at 37 °C. Scale bars: 10 μm (L).

## 3. Results

### 3.1. 2-DG-caused HK inhibition leads to decreased glycolytic but increased mitochondrial ATP synthesis rates

First, we investigated the effect of glycolysis inhibition on mitochondrial oxidative phosphorylation (OXPHOS) in mammalian cervical carcinoma cells (HeLa). HeLa cells are metabolically flexible and thus a suitable model system [39]. The cells were cultivated with quasi physiological concentrations of glucose (5.6 mM) for several passages. The inhibition of glycolysis was initiated by the addition of 2-Deoxy-D-glucose (2-DG) in 5-fold excess (30 mM) to the carbon source glucose (5.6 mM) for up to 5 h. The mitochondrial respiratory function and aerobic glycolysis were then analyzed with an extracellular metabolic flux analyzer (Agilent/Seahorse). Although 2-DG was present all the time, we found a time-dependent inhibitory effect on respiration that was strongest in the first hour. 30 min after addition of 2-DG, respiration, measured as oxygen consumption rates (OCR) were reduced to 63%, but recovered to 75% in the next 30 min and then showed a continuous decrease (Fig. 1A). The decline was stronger than in the control without 2-DG. In parallel, the extracellular acidification rate (ECAR) as a measure of glycolysis, was recorded. The decrease in ECAR was also strongest in the first 30–60 min after 2-DG addition (Fig. 1B). In the control, ECAR finally increased in response to rotenone and antimycin A, suggesting that extracellular acidification was mainly caused by glycolysis and not by TCA cycle activity [40]. This was not the case for the 2-DG probe, suggesting TCA cycle activity instead of glycolytic activity under inhibitory conditions. Next, the mitochondrial stress test was performed. The maximum respiration was measured in the presence of an uncoupler, here trifluoromethoxycarbonyl cyanide phenylhydrazoneane (FCCP), after complex V inhibition with Oligomycin (Fig. 1C). In the time period measured (0.5 h–5 h after initial addition of 2-DG), maximal respiration and spare capacity were reduced (Fig. 1D, E). If 2-DG containing medium was replaced by standard medium for another 2 h after 3 h incubation (= recover), a restoration of maximal respiration to > 90% of the control state was observed. The coupling efficiency was not affected by 2-DG treatment. For metabolic phenotyping, the OCR/ECAR ratio was plotted and revealed a decrease of the extracellular acidification rate as measure for glycolysis due to 2-DG inhibition and as well as attenuation of respiration (Fig. 1F). The fact that there were only slight differences in OCR between 0.5 h and 5 h indicates the use of a different fuel for respiration. In a fuel test, glucose, glutamine and fatty acids were added in combination with inhibitors for the different catabolic pathways (UK5099 for glycolysis; etomoxir for FA oxidation and BPTES for glutamine conversion to glutamate). The result shows that mitochondria became more dependent on glutamine metabolism after glycolysis inhibition, whereas fatty acids were apparently not used as an alternative energy source during measurements (Fig. 1G). This is in accordance to the increased TCA cycle activity observed before (Fig. 1B). To test for ATP synthesis, we included an assay to determine mitochondrial versus glycolytic ATP synthesis as recently established [41]. It revealed that mitochondrial ATP production was increased during 2-DG treatment, while glycolytic ATP production was significantly reduced (Fig. 1H). Notably, 2-DG treatment did not cause a reduction in cell number (Fig. 1I). Next, we determined the cytosolic ATP levels with a genetically encoded fluorescence probe known as ATeam. ATeams consist of the ATP-binding subunit ε of a *Bacillus sp.*, which is located between a fluorescent donor and an acceptor protein [28,42]. After ATP-binding, conformational changes increase Förster resonance energy transfer (FRET) and shorten the fluorescence lifetime of the donor. We exchanged the donor for the fluorescence protein Clover, and the acceptor for mRuby2, which resulted in a Clover-SU-ε-mRuby2 ATeam construct. To monitor cytosolic ATP changes, the fluorescence lifetime of the donor was recorded by fluorescence lifetime imaging microscopy (FLIM). The data show that the cellular ATP level decreased significantly between 0.5 and 1.5 h of glycolysis inhibition (Fig. 1K). After 5 h the ATP values had risen again. Although 2-DG was still present, this was not reflected in the glycolytic ATP production rate values, (Fig. 1H).

### 3.2. The mitochondrial membrane potential is reduced during the attenuation of respiration due to ongoing ATP synthesis

The active complexes I, III and IV pump protons into the intra cristae space and generate an electrochemical gradient or membrane potential ($\Delta\Psi_m$). We asked how the decrease in respiratory activity following glycolysis inhibition affected $\Delta\Psi_m$. We used tetramethylrhodaminethyl ester (TMRE) to measure $\Delta\Psi_m$ under normal conditions and during inhibition of glycolysis and respiration. TMRE is distributed in active mitochondria according to the Nernst equation and in dependence on $\Delta\Psi_m$. An increase in TMRE fluorescence suggests an increased electrochemical gradient or $\Delta\Psi_m$. By means of fluorescence microscopy we determined the mean intensity of TMRE stained mitochondria in single cells and normalized the signal on the MitoTracker™Green signal, which is a mitochondrial mass indicator [43]. To check the contribution of ATP synthase/ATPase to the $\Delta\Psi_m$, oligomycin was added after taking a first round of images (Fig. 1L). Oligomycin treatment resulted in increased $\Delta\Psi_m$, as expected when ATP synthesis was performed before inhibition. We found that 2-DG treatment generally resulted in reduced membrane potential with the

lowest level 1 h after first addition of 2-DG, but already 0.5 h after 2-DG application, $\Delta\Psi_m$ was decreased ($P \leq 0.01$). The $\Delta\Psi_m$ recovered in the next few hours despite the presence of 2-DG (Fig. 1M). The level of respiratory complexes I, II and V did not change during 2-DG treatment, but the core subunit I of complex IV displayed a lower signal in immune-detection at time point 0.5 h (Fig. S1). Reduced complex IV activity could also explain the increase in mitochondrial ROS increase after 0.5 h 2-DG treatment (Fig. 1N), and would result in a decreased $\Delta\Psi_m$. Except for 5 h 2-DG treatment in the presence of oligomycin, the $\Delta\Psi_m$ was always significantly higher than with 2-DG alone, indicating that ATP synthesis driven by the proton motive force was performed during the treatment with 2-DG. We next tested the effect of the ATPase specific inhibitor BMS-199264 [44] under control conditions. While the oligomycin treatment increased the $\Delta\Psi_m$, the BMS-199264 treatment significantly decreased the $\Delta\Psi_m$ ($P \leq 0.001$). This would mean that ATP hydrolysis in the absence of the inhibitor contributes to $\Delta\Psi_m$ and is stopped in the presence of BMS-199264. Accordingly, the decrease in $\Delta\Psi_m$ during 0.5-1.5 h 2-DG treatment might also be explained by inhibition of ATP hydrolysis. Mitochondrial morphology was not significantly affected by 2-DG treatment (Figs. S2, S3).

### 3.3. Ultrastructural analysis of mitochondria

It has been reported that cristae narrow in response to starvation [45]. In order to test whether glycolysis inhibition has the same effect, TEM microscope images of mitochondria in a monolayer of cells incubated with 2-DG were quantitatively analyzed in order to determine the average mitochondrial width, the average cristae width, the number of cristae per µm mitochondrial length, and the cristae shape (Fig. 2 and Fig. S1). No significant differences were found when mitochondrial diameter, and number of cristae per length unit of rod-shaped mitochondria was analyzed in the time frame of 0–3 h after inhibition of glycolysis. However, the cristae width narrowed ($P = 0.035$) when glycolysis was inhibited by 2-DG for 0.5 h (14.45 ± 2 nm) compared to control (15.03 ± 3.6 nm). The effect was reversible and at 1.5 h after 2-DG there was no significant difference between control and 1.5 h 2-DG treatment. So, similar to earlier studies, where cristae thinning was observed under starvation [45], during short term slowdown of respiration an intermediate decrease in the cristae width was detectable (Fig. 2D).

### 3.4. Glycolysis inhibition alters the spatio-temporal organization of single $F_1F_O$ ATP synthase in the mitochondrial inner membrane

Following, we asked whether these slight variations in ultrastructure and changes in complex V activity were correlated with a different spatial organization of the enzyme. $F_1F_O$ ATP synthase is known to be involved in cristae-shaping [12]. Normally, the $F_1F_O$ ATP synthase is located at the tips and rims of cristae [15,16,46]. However, it is not known how strict this localization/organization is and whether it is influenced by different modes of complex V activity (e.g. ATP synthesis vs. ATP hydrolysis). Since submitochondrial resolution was required to monitor possible changes in the spatio-temporal organization of complex V, a recently introduced fluorescence superresolution technique - Tracking and Localization Microscopy (TALM) [19,47] - was used to localize $F_1F_O$ ATP synthase in sub-compartments of the inner membrane. For fluorescence labeling, the HaloTag® was fused with the C-terminus of complex V subunit γ as previously described [47] and a stable cell line was generated expressing this construct. Tagging of subunit γ at this position had no effect on respiratory parameters in a stable transfected cell line (Fig. S4). For the specific labeling, the Tetramethylrhodamine-HaloTag®-Ligand ($TMR^{HTL}$) was added for 20 min as fluorescent substrate for the self-labeling HaloTag®. Unbound $TMR^{HTL}$ substrate was then washed out. Due to the low $TMR^{HTL}$ substrate concentrations (1 nM), the complex V labeling was substoichiometric and individual molecules could be differentiated in the flat, peripheral part of the cells in which the mitochondria form a 2D network [29]. In order to reduce the background fluorescence of out-of-focus emitters, a highly inclined laminated optical sheet (HILO) illumination was used for excitation [32]. For a comprehensive localization map of the complex V, 1000–3000 images were recorded (frame rate 33 Hz). Fluorescence signals of individual molecules were fitted

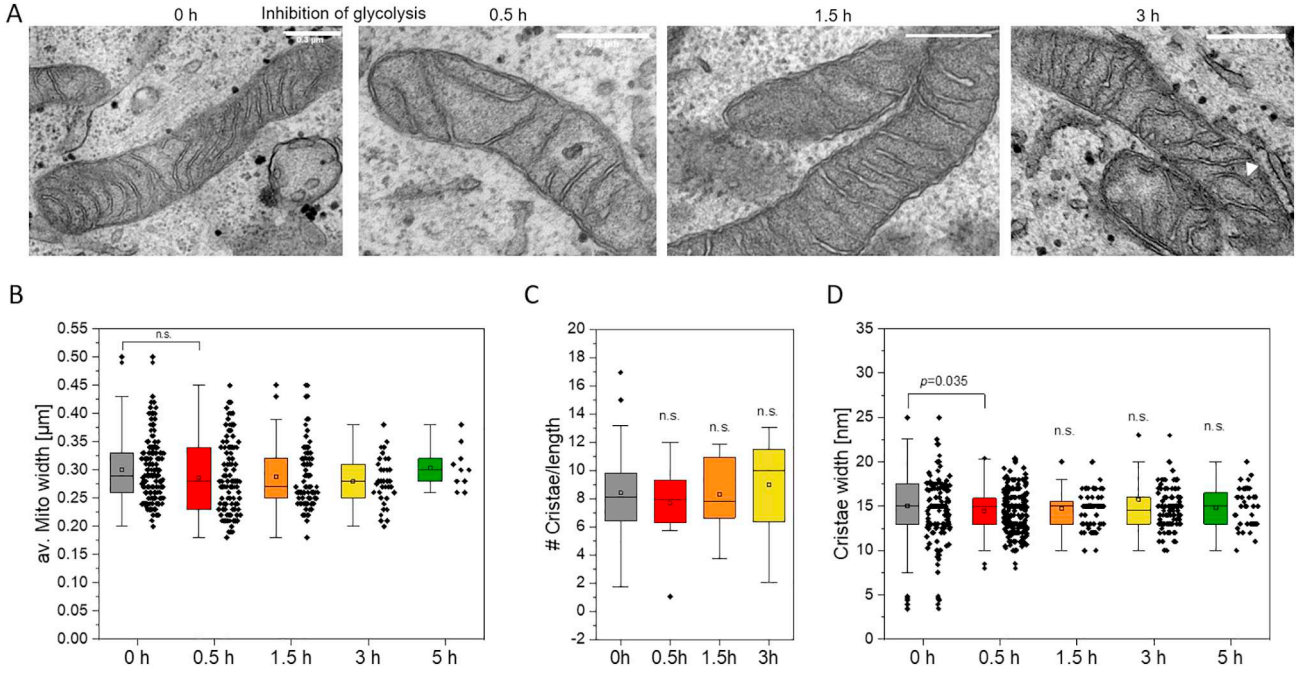


**Fig. 2.** Ultrastructural analysis of mitochondria from glycolytic and glycolysis inhibited cells. (A) Transmission electron microscopy (TEM) images of single mitochondria at different time points after 2-DG application and metabolic switch. (B) Average mitochondrial width ($N = 2$ independent specimen; $n = 57$ (0 h), $n = 40$ (30 min), $n = 40$ (1.5 h), $n = 36$ (3–5 h) mitochondria). (C) Average cristae width ($n = 224$ cristae, 0 h; $n = 288$ cristae, 0.5 h; $n = 290$ cristae, 1.5 h; $n = 112$ cristae, 3 h), (D) Cristae per length of mitochondrion ($\mu m^{-1}$) ($n = 26$, 0 h; $n = 13$, 0.5 h; $n = 19$, 1.5 h; $n = 15$, 3 h). Scale bars: 0.3 µm (A). ANOVA test, $P \leq 0.001^{***}$.

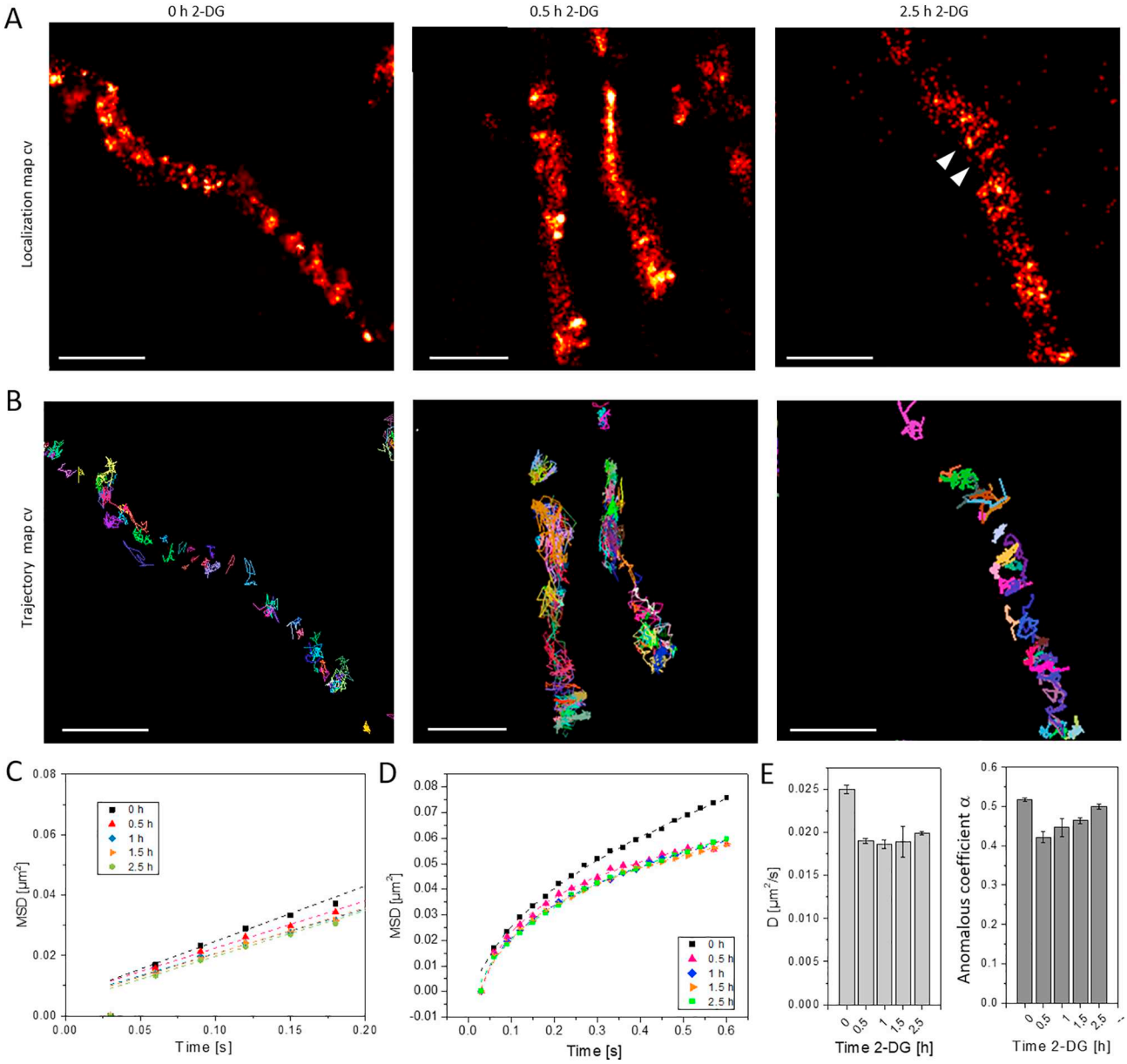


**Fig. 3.** The localization and dynamics of ATP synthase and ATPase are different. (A) Effects of 2-DG (2-deoxyglucose) on the localization pattern of $F_1F_O$ ATP synthase at different times after 2-DG addition. Localization maps of the single $F_1F_O$ ATP synthase in mitochondria resulting from the summation of up to 3000 images. The application of a Gaussian fit on the PSF of the single molecules resulted in point localized $F_1F_O$ ATP synthase single molecules. Recording rate: 30 fps (33 Hz). Point localizations are false color-coded in *Hot*. (B) Mobility of ATP synthase at different times after onset of glycolysis inhibition with 2-DG. The panels show trajectory maps of the $F_1F_O$ ATP synthase in individual mitochondria resulting from time series between 48 and 96 s (1600–3000 frames), see Movie S1, Movie S2 and Movie S3 in supplementary information. Trajectories of the $F_1F_O$ ATP synthase were generated by using the Multi-Target-Tracing-Tool (MTT). Every single trajectory in one color. (C) Mean square displacement (MSD) diagram showing the linear increase of the MSD in short-term (200 ms) diffusion times. (D) Complete MSD plots covering mean square displacements in the range between 2 and 20 steps (600 ms). (E) Diffusion coefficients and anomalous coefficients calculated from MSD/time diagrams according to Eq. (2). Scale bar: 1 µm (A, B).

with a 2D Gaussian distribution using a calculated point spread function as reference to obtain the precise localization for all particles. In this way, we produced localization maps for complex V at different times after glycolysis inhibition (Fig. 3A). Under control conditions, complex V showed a structured distribution along the longitudinal axis of a mitochondrion (Fig. 3A, left panel). During the first 2 h of glycolysis inhibition, the distribution profile changed to a more dispersed one. 2.5 h after addition of 2-DG, a regular, striped distribution pattern of the $F_1F_O$ ATP synthase was visible again in certain areas of the mitochondria (Fig. 3A, right panel, white arrowhead).

A change in the localization pattern must be associated with a dynamic rearrangement of the $F_1F_O$ ATP synthase. To test this, the dynamics of the fluorescence-labeled $F_1F_O$ ATP synthase in mitochondria in living cells was determined by single molecule tracking microscopy. For this purpose, trajectories of the mobile $F_1F_O$ ATP synthase were generated: Localized particles in subsequent frames were linked if they were found within a defined maximum distance and if they had the same biophysical footprint (such as intensity). The multi-target tracer (MTT) algorithm [48] was used to identify and connect particles. Individual trajectories were colored in different colors (Fig. S5A, B). By overlaying trajectories, which were color-coded according to their temporal occurrence, it was possible to determine whether the mitochondria had moved during the recording time. Data from moving mitochondria have not been considered (Fig. S5C). The dynamics of the

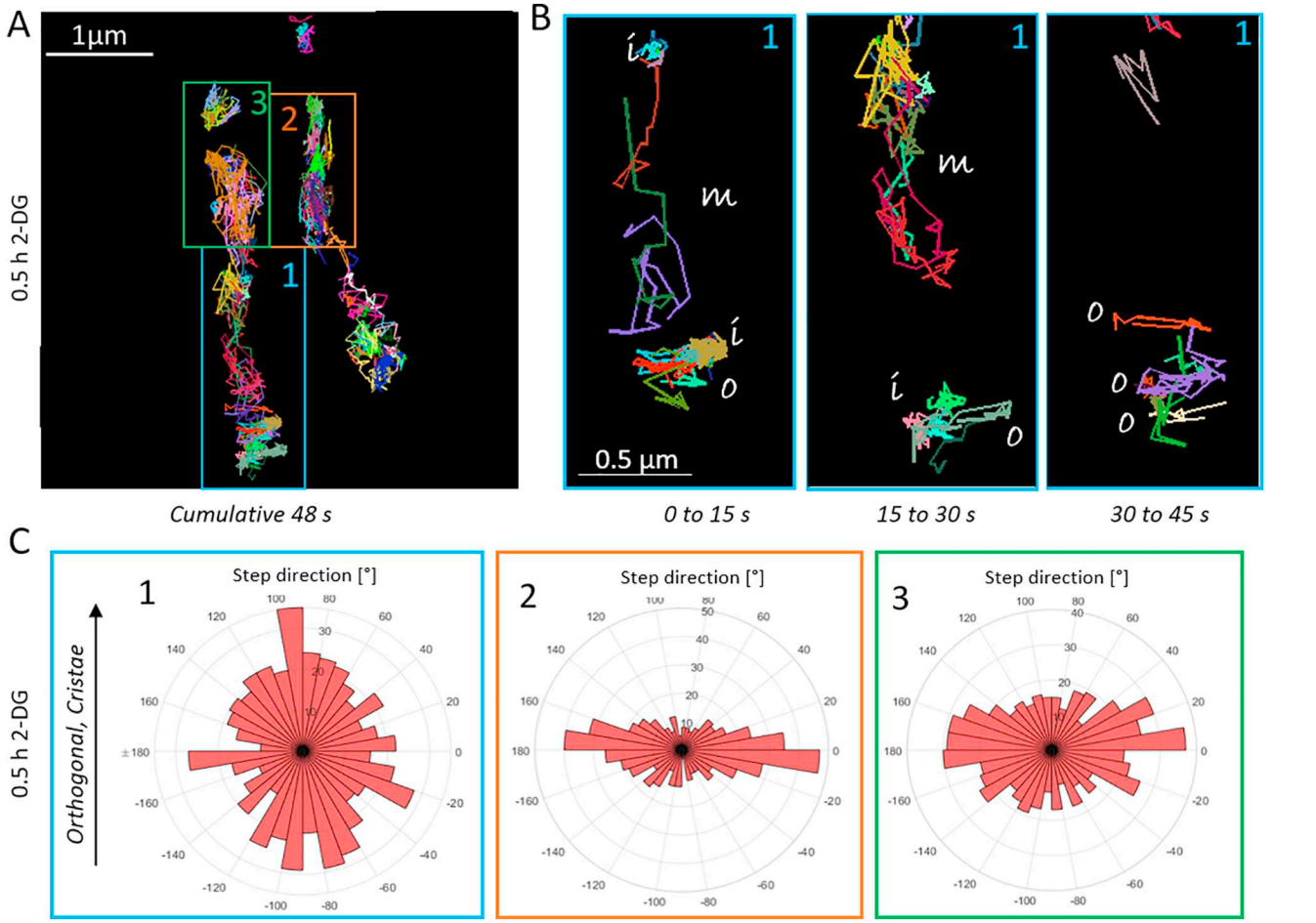


**Fig. 4.** Quantification of the dynamics and directionality of $F_1F_O$ ATP synthase. (A) Trajectory map of the $F_1F_O$ ATP synthase in two mitochondria after 0.5 h incubation with 2-DG. A cumulative image with trajectories from a 1605 image film lasting 48 s is displayed. (B) Detailed view of the individual trajectories from the framed part #1 of (A), each image shows the trajectories of 500 subsequent images (15 s). m: unrestricted movement, o: Diffusion orthogonal to the longitudinal axis of the mitochondrion, i: immobile molecules. Individual trajectories are displayed in different colors; only trajectories with a minimum duration of 180 ms are displayed. (C) Analysis of the step directions with respect to the longitudinal axis ( ± 180° and 0°) and the orthogonal axis (−90° and +90°) represented on a graduated disk. The direction of the trajectories from the framed areas of interest #1, 2 and 3 of (B) are shown here in the degree window. For the determination of directionality, 5 successive steps were integrated.

fluorescent $F_1F_O$ ATP synthase particles were recorded over a period of 32 s to 96 s (1000 to 3000 images; 33 Hz) at different times of glycolysis inhibition (0 h, 0.5 h, 1.5 h and 2.5 h) and cumulative trajectory maps were generated. The movement of complex V in tubular single mitochondria is shown in Fig. 4B as a cumulative superposition of recorded trajectories for the times 0 h, 0.5 h and 2.5 h after 2-DG application.

Under normal respiratory conditions, complex V predominatly shows restricted movement in cristae, visible as orthogonal trajectories. This has already been comprehensively analyzed earlier [19,49]. However, within 0.5 h after glycolysis inhibition, the trajectory pattern of the $F_1F_O$-ATP synthase became more diffuse (Fig. 3B, middle panel). After 2.5 h more orthogonal trajectories appeared again (arrowhead Fig. 3B, right panel). In order to quantify this, mean square displacement diagrams (MSD) were generated (Fig. S6). If only the short-term diffusion (2–5 step sliding intervals) was analyzed, the MSD increased linearly over time for all conditions and time points (Fig. 3C). However, in the presence of 2-DG and glycolysis inhibition, MSD were lower, suggesting reduced complex V movement. When the MSDs were recorded for 2–20 steps, the relation between MSD and time was no longer linear but attenuated, indicating restricted or anomalous diffusion (Fig. 3D). We then calculated the diffusion coefficients from the MSD according to the formula (2) in section 2.10:

Individual MSD/time diagrams for the different time points of 2-DG inhibition are shown in Fig. S6. The total number of trajectories analyzed per condition is listed in supplementary Table 1.

The calculated diffusion coefficients of complex V in normal cells and in inhibited cells were clearly different and showed a decrease of the average mobility in the latter (Fig. 3E). At the same time, the coefficient α decreased, which correlated with an increased anomalous diffusion. In order to dissect this in detail, we determined the directionality of movement of complex.

### *3.5. Mitochondrial ATPase has a different temporal footprint than ATP synthase*

As described earlier, mobile complex V in cristae has a preferred direction of motion orthogonal to the longitudinal axis of the mitochondria [19,]. This is related to the almost exclusive localization of ATP synthase in cristae [49,51,52]. When glycolysis was inhibited and ATPase activity reduced, this motion pattern was clearly changed (Fig. 3B, middle panel). To dissect these changes in more detail, the trajectory map of complex V in mitochondria of an exemplary cell was divided into three areas (#1, blue frame; #2, orange frame; #3, green frame) (Fig. 4A). In area #1 (0s –15 s), trajectories with long step lengths indicate the presence of unrestricted mobile particles, moving in all directions (marked with **m**). In the upper part, a trajectory of an immobile molecule is shown (light blue), marked with **I** (Fig. 4B, left

panel, # frame 1). In the lower part, several particles showed an orthogonal direction of motion typical for diffusion in cristae membranes (indicated as **o**). During the next 15 s, further free moving particles appeared in the upper part (**m**), while orthogonally moving (**o**) and immobile molecules (**i**) continued to dominate in the lower part (see Fig. 4B, middle panel, frame #1). Between 30 s and 45 s, mainly orthogonal trajectories were registered in the lower part (Fig. 4B, right panel, frame #1). Next, we quantified the motion in relation to the longitudinal axis of the mitochondria. Therefore, the direction of the successive steps of a moving single molecule was described by a vector. The relative shares of direction were expressed in degree [°] and plotted on a circular disc. The longitudinal axis of a mitochondrion was assigned as covering ± 180° and 0° and the orthogonal axis as −90° and 90°. First, the longitudinal axis of a mitochondrion was drawn manually. Curved mitochondria first required a linearization. For this purpose, the longitudinal axis of a curved mitochondrion was stretched to linearity in order to generate a transformation matrix (Fig. S7C). For the vector analysis, the integrated change of direction between the first and the fifth step was determined and then plotted on the directionality disk (Fig. S7D). This analysis also made it possible to determine the diffusion coefficients *D* for the movement along the longitudinal axis and in the orthogonal direction independently of each other by generating separate MSDs (Fig. S8). The derivation of diffusion coefficients in dependence on time shows that the physical constraint imposed by the cristae architecture reduces the mobility (lower $D_{orthog.}$) compared to movement along the tubular shape of the IBM (Fig. S8E).

The directional analysis of the areas framed in Fig. 4A shows that in the area #1 trajectories with orthogonal direction (−90° and 90°) prevail. This indicates an organization in the cristae sheet. In contrast, the trajectories in the areas #2 and #3 are different with a strong share of steps in the longitudinal direction (Fig. 4C). This would be consistent, for example, with the movement in the tubular IBM, since in a tubular structure the longitudinal direction ( ± 180° and 0°) always prevails due to geometric reasons. Moreover, confined longitudinal trajectories can also represent dimeric complex V at cristae edges.

We next performed a global directionality analysis for the motion of ATP synthase/hydrolase under all conditions. The respective trajectory maps that were analyzed are shown in Fig. 5A. Already visible from the maps is the distinct pattern at time point 0.5 h of 2-DG inhibition of glycolysis and respiration corresponding with the metabolic switch. The directionality was quantified as described and results are displayed on directionality discs. As the distribution shows, orthogonal/perpendicular movement dominated at 0 h (Fig. 5B). Between 0.5 h to 1.5 h after 2-DG induced enhanced ATP synthesis, the vector analysis of directionality suggests an increased share of longitudinal movement. After 2.5 h, corresponding with a recovery of mitochondrial physiology and ATP hydrolase activity, the preferential movement of complex V reverted back to an orthogonal orientation. We then performed MSD analysis in the short time range (2–5 frames) for longitudinal and orthogonal movement separately (Fig. 5C). During the first 0.5 h, MSDs in the orthogonal direction was lower than mean square displacements in the longitudinal direction. At 2.5 h, the MSD in longitudinal and orthogonal direction did not differ any more (Fig. 5C). The different mobility behavior of ATP synthase and ATPase resulted in different

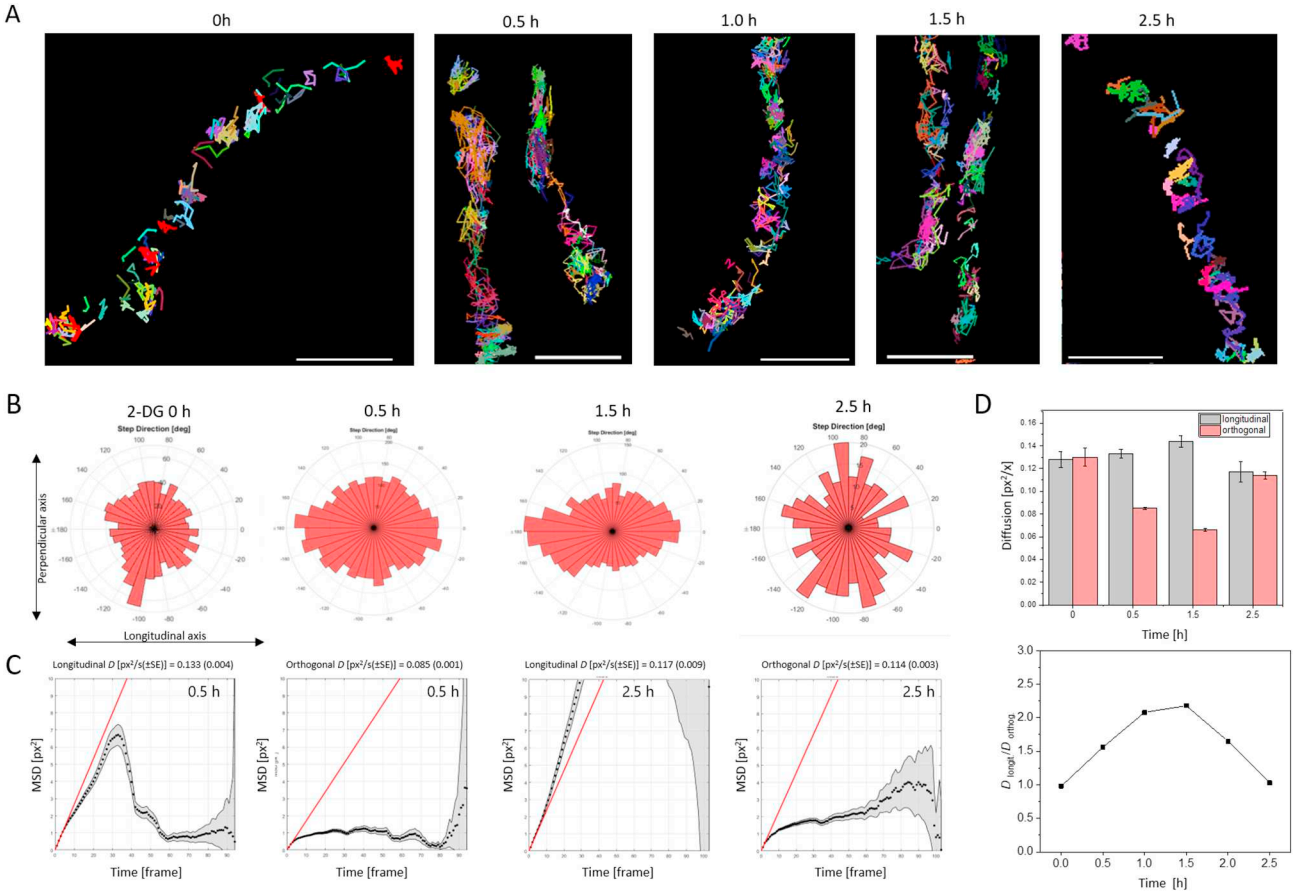


**Fig. 5.** The diffusion of $F_1F_O$ ATP synthase in cristae is reduced when glycolysis is inhibited. (A) Exemplary cumulative trajectory maps of ATP synthase in mitochondria at different times after starting glycolysis inhibition. Time 0.5–1.5 h corresponds to inhibition of ATPase activity. (B) Directionality of ATP synthase movement in mitochondria shown in (A). (C) Mean square displacements (MSDs) for longitudinal and orthogonal movement at 0.5 h and 2.5 h 2-DG treatment. (D) Diffusion coefficients *D* for longitudinal and orthogonal displacements at different time points. The ratio of the diffusion coefficients $D_{longit.}/D_{orthog.}$ is plotted to demonstrate the difference exemplary.

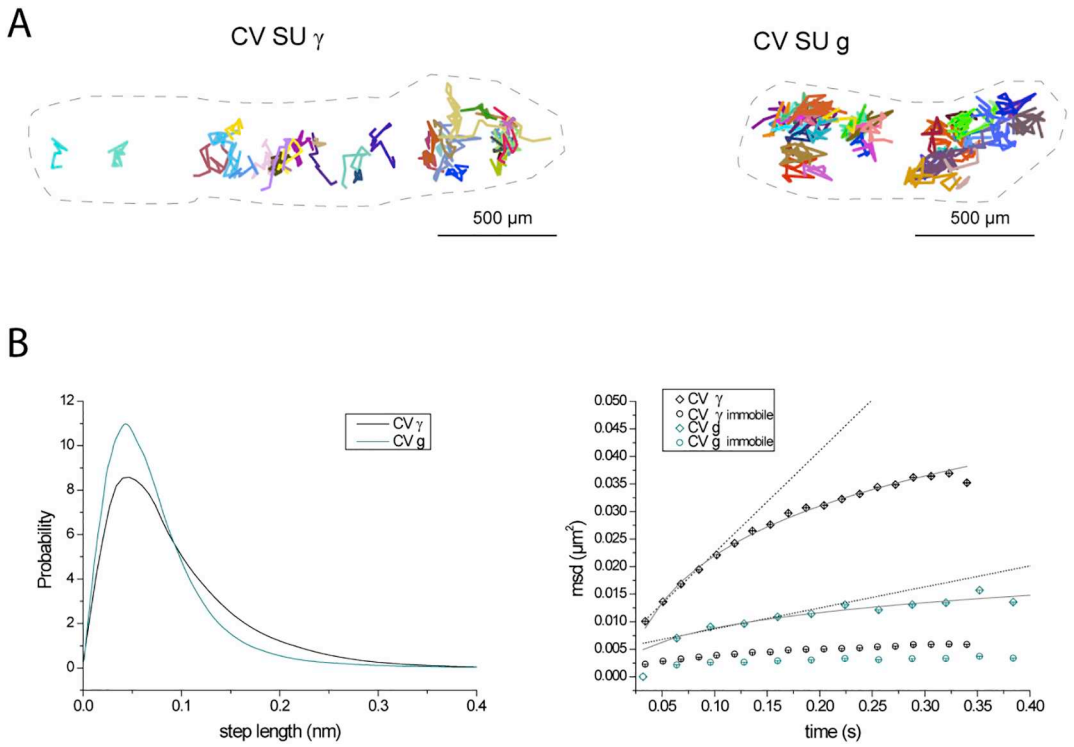


**Fig. 6.** Dimers of complex V display a very low mobility. (A) Trajectory maps of ATP synthase labeled at subunits γ and g in single mitochondria. The grey line was drawn to indicate the mitochondria. Lines in color represent individual trajectories of single molecules. (B) Step length histograms and means square displacements (MSD) are plotted. The MSD of the long range diffusion was fitted assuming anomalous diffusion (α = 0.069 for CV SU γ and 0.042 for CV SU g). For subunit γ labeled ATP synthase, 12,277 trajectories were analyzed, for subunit g 22,811 trajectories.

diffusion coefficients *D* for longitudinal and orthogonal motion (Fig. 5D). The diffusion in the orthogonal direction was lowest at 1 h to 1.5 h corresponding with decreased ATPase activity. The directionality analysis of > 15,000 steps of ATP synthase/hydrolase in mitochondria at different time points ($N = 2$ independent assays) essentially confirmed the results (Fig. S9). The directional diagrams for the movement of ATP synthase were similar before and after 2.5 h of glycolysis inhibition, while at 0.5 h–1.5 h (increased ATP synthase activity) the amount of orthogonal traces was reduced. In our opinion, this clearly indicates a change in the spatio-temporal organization of ATP synthase compared to ATP hydrolase. It appears that the average mobility of complex V in cristae decreased when ATP synthesis was.

### 3.6. ATP synthase dimers display lower mobility than the average pool of ATP synthase

In order to dissect dimeric complex V by its tracking behavior, we tagged complex V at SUg with the HaloTag for labeling. SUg is suggested to trigger ATP synthase dimerization together with SUe [53,54]. Cells were transiently transfected with SUe-HaloTag and labeled with 0.5 nM $TMR^{HTL}$. We recorded trajectories of ATP synthase labeled at SUg and SUγ in direct comparison (Fig. 6A). The trajectory maps of complex V in single mitochondria show a clear difference with more molecules displaying shorter step length and a significantly lower mean square displacement of complex V labeled at SUg (Fig. 6B). For long range diffusion, we calculated $D_{SUg} = 0.054 \pm 0.039$ [SD] µm/s and $D_{SU_\gamma} = 0.033 \pm 0.039$ [SD] µm/s. While complex V labeled at SUγ does not discriminate between monomers, dimers and oligomers and thus represents the entire population, labeling SUg probably will mainly discern dimeric and oligomeric complex V. Short range diffusion analysis revealed that, dimers/oligomers of complex V are almost immobile ($D_{\text{short range}} = 0.018 \pm 0.005$ [SD] µm/s compared to $D_{\text{short range}} = 0.046 \pm 0.002$ [SD] µm/s for SUg), localized at the cristae rims.

### 3.7. Inhibition of ATPase activity results in decreased mobility of complex V

In order to test, whether inhibition of ATPase activity affects the mobility of the enzyme, we inhibited ATPase activity with the specific inhibitor BMS-199264 [44]. If inhibition of ATPase activity under 2-DG conditions was the cause for the decrease in diffusion, we would also expect a decrease in mobility upon BMS-199264 treatment. Thus, cells expressing the Halo-Tagged SUγ of ATP synthase were exposed to 5 µM BMS-199264. This treatment caused a decrease in the $\Delta\Psi_m$ (Fig. 1M), which can be explained if ATP synthesis activity continued while ATPase activity stopped. Indeed, we found decreased mobility of ATP synthase when cells were incubated with BMS-199264 alone or together with 2-DG for 0.5 h (Fig. 7A). In parallel, a significant fraction of quasi immobile particles appeared in the trajectory map (Fig. 7B, pink arrowheads, right panel). Thus, inhibition of ATPase activity obviously decreases the overall mobility of the enzyme. The localization map reminds of the map of SUg (Fig. 6A).

### 3.8. Knockdown of inhibitory factor 1 IF1 results in an increase of complex V mobility under normal and 2-DG conditions

We next asked, how ablation of inhibitory factor 1 (IF1) would impact on the mobility of ATP synthase. IF1 binds to ATP synthase dimers in the groove between α-helices of subunits α and β in the $F_1$ head [55] and likely is involved in dimer/oligomer formation [56]. It can be expected that knockdown of IF1 will result in increased ATP hydrolysis, resulting in increased mobility of the enzyme. If the hypothesis is correct that cells treated with 2-DG are IF1-blocked and possess more oligomeric ATPase, in the absence of IF1 the mobility of the overall complex V population should increase. We first generated IF1-KO knockout cells by the CRISPR/Cas9 technology. Puromycin-resistant clones were subjected to immunoblot analysis to verify knockout of the target gene (Fig. 8A). Four knockout clones were identified, tracking studies were continued with clone #8. IF1-KO cells were

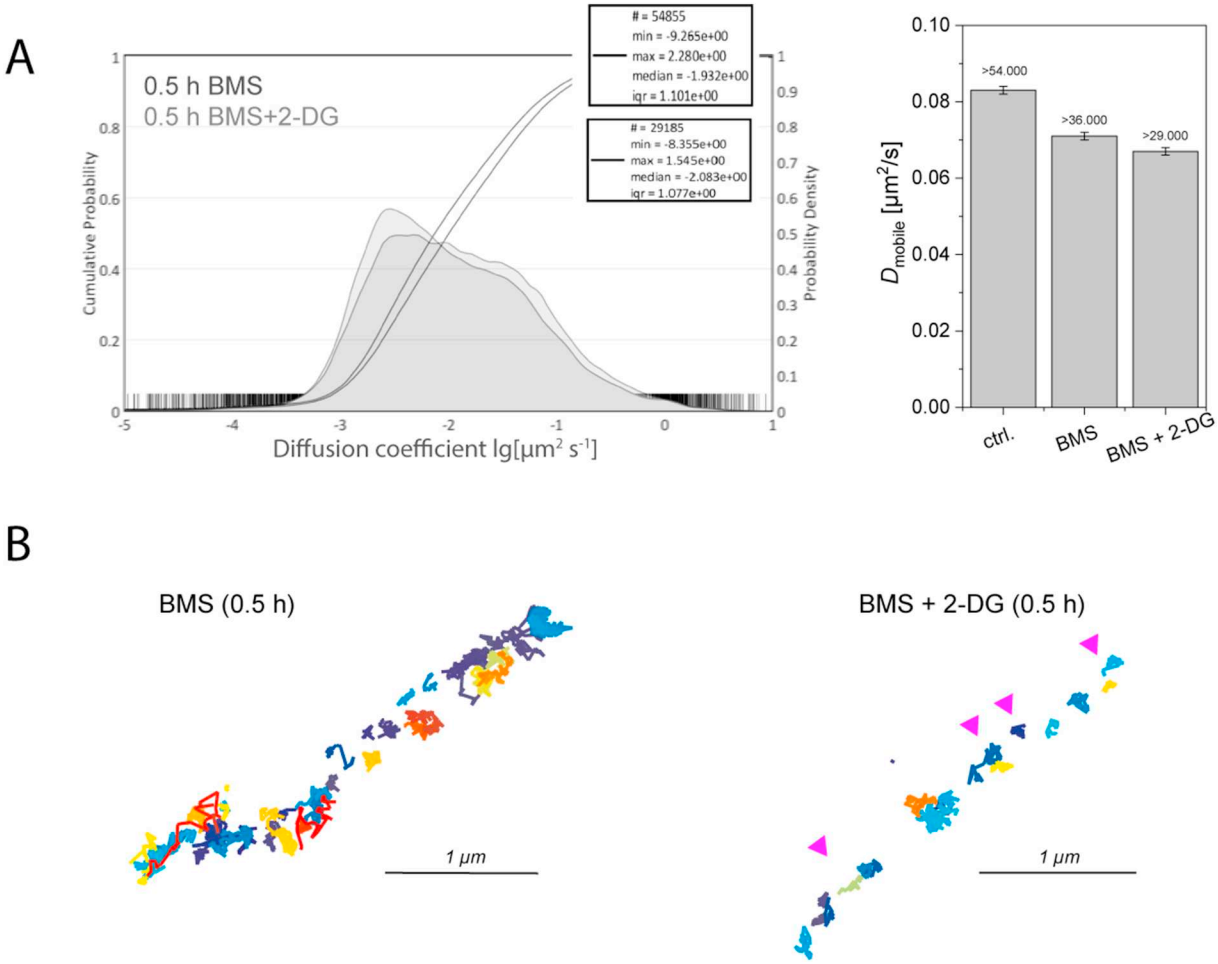


**Fig. 7.** Inhibition of ATP hydrolysis activity results in decreased mobility of the ATP synthase population. (A) Histogram of diffusion coefficients for ATP synthase under control conditions (5.6 mM Glucose, no inhibition), in the presence of BMS-199264 (5 μM) and BMS-199264 treated in addition with 2-DG for 0.5 h. The cumulative probabilities are plotted. Peaks from left to right: BMS + 2-DG, BMS. Data from $N = 3$ biological replicates. In the right graph, the median diffusion coefficients are plotted. Numbers at the top of the columns indicate the number of analyzed trajectories. No errors are shown, since all trajectories ($N = 3$ biological replicates, > 20 cells) were analyzed in a batch procedure. (B) Trajectory map of mitochondria from an BMS treated cells and a BMS plus 2-DG treated cell, both 0.5 h after application of the inhibitors. Frame rate 32 ms, 4000 frames in total recorded, superimposition of all trajectories during measurement. Red: early trajectories (frames 0–500), dark blue: late trajectories (frames 3500–4000).

transiently transfected with CV-SU γ-Halo Tag, labeled with $TMR^{HTL}$ and imaged at a TIRF-fluorescence microscope. 4000 frames per region of interest were recorded with a frame rate of 32 ms/frame. The following conditions were compared: control cells with glucose supply (ctrl.), IF1-KO cells and IF1-KO cells treated with 2-DG (30 mM for 0.5 h). The mobility of ATP synthase was determined with the MTT tracker and the cumulative probability of the diffusion coefficients $D$ plotted (Fig. 8B). The peaks from left to right indicate ctrl., IF1-KO and IF1-KO + 2-DG conditions. The corresponding median $D$ were then plotted for comparison. Clearly, ATP synthase in IF1-KO cells displayed a higher mobility than in control cells. This is expected, either when more complex V monomers are present, respectively less complex oligomers and/or ATPase activity is increased, according to our hypothesis. Interestingly, 2-DG treatment for 0.5 h here further resulted in increased mobility of complex V. We next analyzed the changes in ATP synthase monomers, dimers and oligomers under the different conditions.

### *3.9. Glycolytic inhibition results in a higher proportion of dimer-bound IF1*

So far, our data suggested that the spatio-temporal re-organization of complex V observed under inhibitory conditions is due to bioenergetic changes in combination with changes in the molecular assembly. Therefore, we determined whether the amount of subunit e, which is known to contribute to dimerization of the complex V [57,58] was changed during 2-DG treatment (ATP hydrolyzing conditions). We compared levels of SUe with levels of SUβ. VDAC, an outer membrane protein, was analyzed as a loading control. At 0.5 h, the level of SUe was significantly ($P = 0.0077$) reduced relative to the level of VDAC after inhibition of glycolysis (Fig. 9A). In parallel, levels of subunit β were determined. After 3 h, the relative protein level of complex V appeared to be decreased ($N = 5$, normalization on VDAC), however, this was not confirmed in a different batch of experiments (Fig. S1). When SUe was related to SUβ, the lowest ratio of SUe/SUβ was observed at time point 0.5 h after inhibition of glycolysis.

To complement the results, we performed BN-PAGE to separate oligomers, dimers and monomers of complex V at the different time points after glycolysis inhibition. We found a relative decrease of dimers compared to monomers after 0.5 h of 2-DG treatment (Fig. 9B). Oligomers apparently decreased between 0.5 h and 1.5 h after glycolysis inhibition, but quantification was difficult (Fig. S10A). Next, we tested, whether IF1, the inhibitory factor 1 of ATPase which is upregulated in cancer cells [59], would bind to monomers and dimers during the inhibition of glycolysis. This was indeed the case, we found IF1 associated with monomeric and dimeric ATP synthase. Binding of IF1 obviously is not exclusive to dimers. We then normalized the

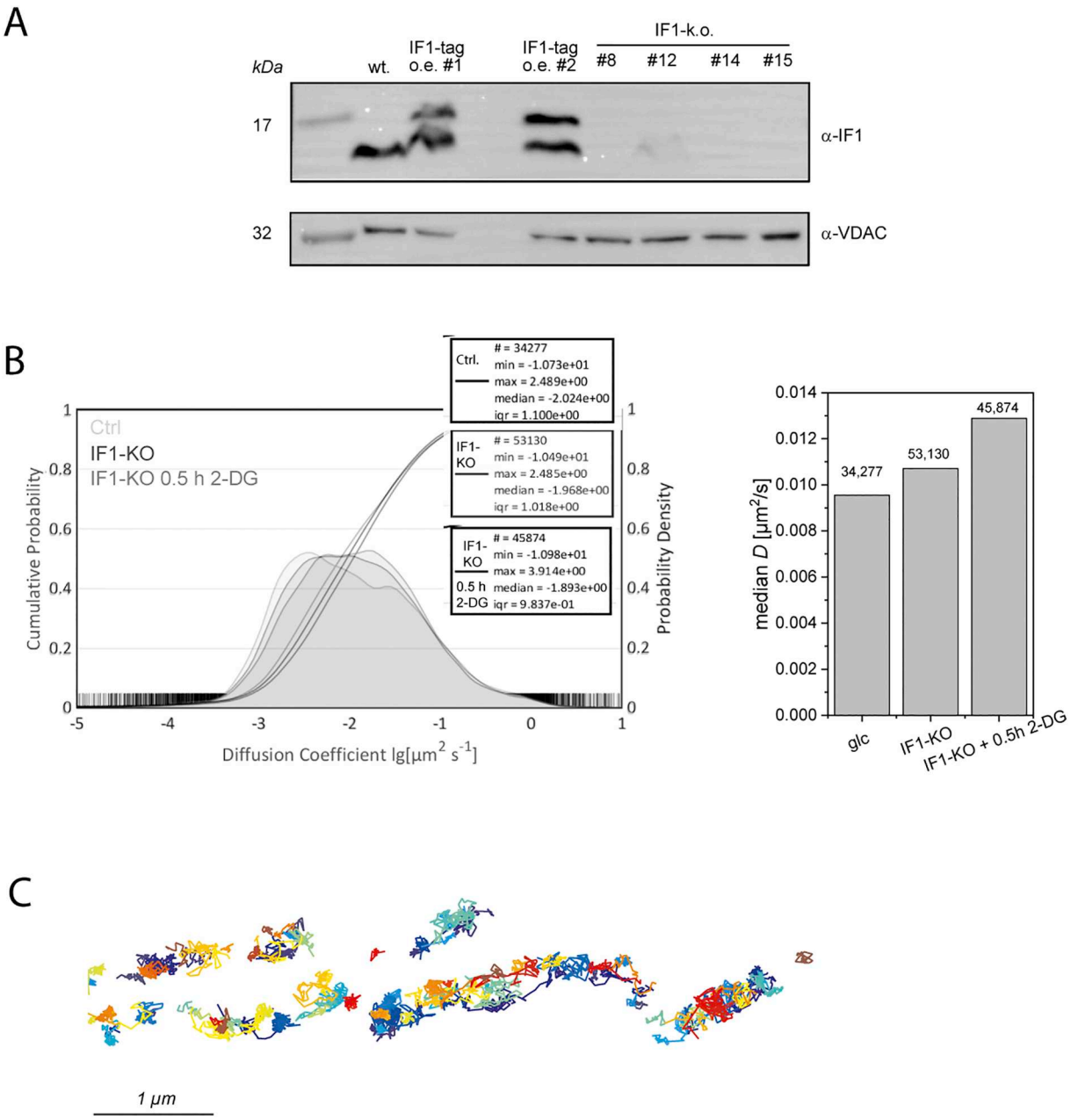


**Fig. 8.** ATP synthase mobility increases in 2-DG-treated IF1-KO cells. (A) Candidate IF1 knock-out clones of human cervical carcinoma cells were subjected to immunoblot analysis with antibodies against IF1 and the mitochondrial marker protein VDAC. (B) Histogram of diffusion coefficients for ATP synthase under control conditions (5.6 mM Glucose, no inhibition), in IF1-KO cells and in IF1-KO cells treated with 2-DG for 0.5 h. The cumulative probabilities are plotted. Peaks from left to right: ctrl., IF1-KO, IF1-KO + 2-DG. Boxes show the number of trajectories analyzed, and the statistical values (minimal *D*, maximal *D*, median, iqr: interquartile range). Data from $N = 3$ biological replicates. In the right graph, the diffusion coefficients are plotted. Numbers at the top of the columns indicate the number of analyzed trajectories. No errors are shown, since all trajectories ($N = 3$ biological replicates, > 20 cells) were analyzed in a batch procedure. (C) Trajectory map of mitochondria from an IF1-KO cell treated with 2-DG. Frame rate 32 ms, 4000 frames. Red: early trajectories (frames 0–500), dark blue: late trajectories (frames 3500–4000).

calculated IF1 dimer/monomer ratio to the SUß dimer/monomer ratio. The proportion of IF1 bound to dimers tended to increase relative to the binding to monomers (Fig. 9B, right panel). Unfortunately, we could not quantify changes in IF1 binding to the oligomeric complex V.

Our data suggest that glycolysis inhibition was accompanied by a relative increase in the ratio of dimers/monomers that have bound IF1.

## 4. Discussion

The aim of this study was to check if the activity mode of mitochondrial complex V, either ATP synthesis or ATP hydrolysis, is associated with a specific spatio-temporal organization. Complex V of oxidative phosphorylation was suggested to work as an ATP synthase under physiological conditions, but under certain circumstances, e.g. under ischemic or in cancer cells, it can function as an ATPase. To alter complex V activity, we decided to inhibit glycolysis with 2-DG treatment. As recently demonstrated, the inhibition of HK by 2-DG had a strong and fast effect on mitochondrial ATP metabolism [42]. Also, one advantage of this strategy was that respiration and ATP synthase were not directly inhibited. Our measurements suggest that before 2-DG administration a subpopulation of the complex V worked in reverse mode. However, most surprisingly, mitochondrial ATP synthesis took

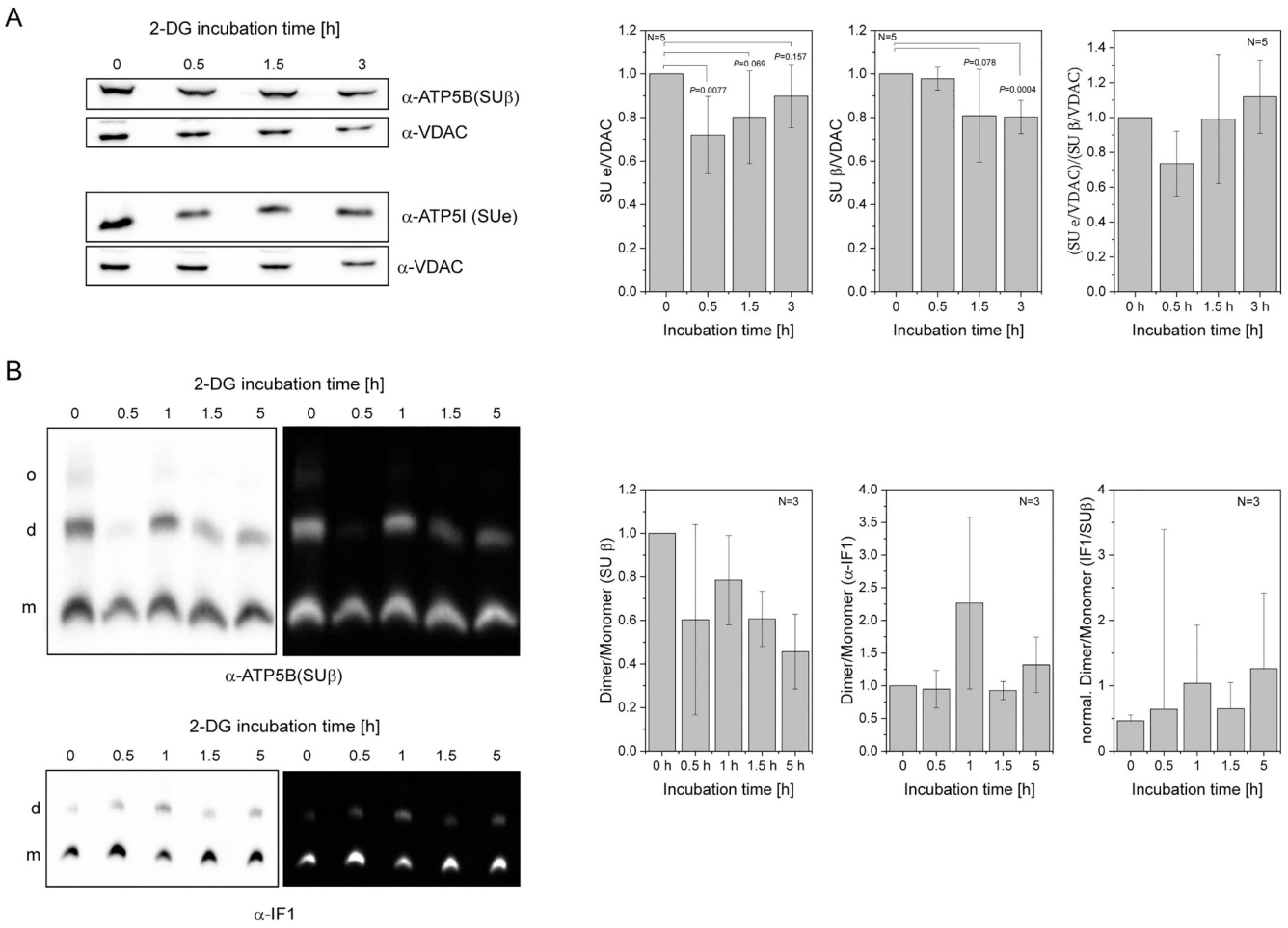


**Fig. 9.** Glycolytic inhibition results in a relative higher proportion of dimer-bound IF1. (A) Relative protein levels of SUe of ATP synthase/complex V (AB: ATP5I) and SU-β of ATP synthase (AB: ATP5B) and their ratio normalized to VDAC (AB: VDAC) at different times during glycolysis inhibition ($N = 5$). SDS-PAGE with immunostaining as indicated. Statistics: ANOVA test, SD shown. (B) BN-PAGE separation of complex V oligomers, dimers, and monomers and detection of ATP complexes by immunostaining with α-ATP5B (anti-SU-β) and with α-IF1 (anti-IF1). Abbreviations: o: oligomers d: dimers, m: monomers. Images are also shown in inverse mode (right panel). No oligomers were detected with α-IF1. The dimer/monomer ratio was calculated for each gel and averaged (left and middle graph). Right graph: Relative binding of IF1 to complex V dimers/monomers (normalized to the SU β signal). Mean values of three independent replicates were used. Calculation of error propagation see statistics sections.

place at the same time and continued during 2-DG inhibition as the oligomycin effect suggests. Indeed, a similar transient increase of matrix ATP levels upon 2-DG induced glucose deprivation was observed earlier [42], followed by ATP decrease. During 2-DG treatment, the mitochondrial membrane potential decreased, probably due to reduced proton pumping. BMS-199264, an ATP hydrolase inhibitor, also decreased $\Delta\Psi_m$, suggesting that ATP hydrolysis activity was present before. Based on this data we suggest that two populations of complex V with different function can be present at the same time, probably in different sub-compartments: ATPase in the cristae sheet and ATP synthase in more confined (cristae edges). Reverse proton pumping by ATP hydrolysis function could be physiologically useful to provide a membrane potential, e.g. for import processes [60].

Because mitochondria switched to another fuel source, the effects of glucose depletion on ATP synthase/hydrolase were only short-term (0.5 to 1.5 h) and reversible. This reversibility enabled us to study the effects of the induced shift on the organization of complex V. We determined the spatio-temporal organization of complex V during the time window for which we had evidence of altered ATPase activity and compared it with the conditions in which ATP hydrolysis was blocked or released. To block ATPase activity, we used the inhibitor BMS-199264 [44] and to study the effect of a release of inhibition of ATPase, we used an IF1-KO cell line. IF1, the inhibitor factor 1 is the physiological master regulator of ATPase activity [56]. It is widely accepted that IF1 blocks the hydrolysis function [61] but more recent data also suggest an inhibitory effect on the ATP synthesis mode [59]. A microscopy method based on single molecule tracking and localization [19] was used to dissect the organization of ATP synthase molecules in mitochondria *in situ* and to generate detailed maps of the localization and dynamics of complex V under different conditions. Under normal conditions, $F_1F_O$ ATP synthase is confined in cristae in terms of localization and mobility [19,49,51,62], which manifests itself in restricted mobility. Significant proportion of complex V displays orthogonal trajectories in the cristae sheet, performing ATP hydrolysis. Here we report that this specific spatio-temporal arrangement has changed with altered complex V activity. A thorough analysis of the mobility patterns including the analysis of the directionality of the movement showed that the confined mobile fraction of the ATP synthase in the cristae increased and the orthogonal directional dependence was lost at the same time. In addition, we found a reduction in cristae width. A narrowing of the cristae in response to starvation has been described earlier [13,45]. The ultrastructural changes under starvation were mainly attributed to the changes in OPA1 levels, whereby the contribution of complex V was not discussed [45]. However, no changes in OPA1 levels were reported for 2-DG-induced metabolic starvation [23], leading us to conclude that an alteration in the complex V dimers/monomer ratio was mainly

responsible for the mild and reversible effect on cristae narrowing. Since this would decrease the volume, more efficient coupling is expected [63]. In addition, we found a tendency of more IF1 binding to complex V dimers under this condition. IF1 was shown to promote dimerization of the mitochondrial $F_1F_O$ ATP synthase [61]. In IF1-KO cells, ATP synthase displayed a higher mobility, while in BMS-199264 treated cells (inhibition of ATP hydrolysis), the mobility decreased. Together, this data support the hypothesis that ATPase activity is associated with a different localization and organizational state in the inner mitochondrial membrane. We suggest that the assembly of ATP synthase that is usually organized in a regular dimer/oligomer structure at the cristae rims [16,52,64–66], thereby shaping the cristae curvature [12,67,68], is associated with ATP synthase. Under 2-DG treatment, the loss of orthogonal trajectories and the decrease of complex V mobility in the cristae sheet suggests that immobile dimeric and oligomeric $F_1F_O$ ATP synthases remained. The observed cristae narrowing is in accordance with this, since a change of the cristae architecture is a frequent outcome when the oligomerization of ATP synthase is altered due to various conditions [13,14,17,63,69–71]. In this context, we provide for the first time data on the dynamic spatio-temporal organization of $F_1F_O$ ATP synthase in living cells.

In summary, our observations suggest that the specific spatio-temporal organization of complex V in subcompartments of the inner mitochondrial membrane may be essential for its respective function, namely either ATP synthesis or ATP hydrolysis. Obviously, complex V displays a comparable dynamic organization as the respiratory complexes which assemble into supercomplexes for functional adaptation [72,73]. It can be speculated that the arrangement of the complex V dimers in rows that form the cristae, which is obviously advantageous for optimal function as ATP synthase [46], is not necessarily also the typical arrangement for the ATPase function. However, to finally ascertain this, the specific activity of $F_1F_O$ ATP synthase would have to be visualized with submitochondrial resolution *in situ*.

## 5. Conclusions

Mitochondrial $F_1F_O$ ATP synthase has several functions: in ATP synthesis, cristae shaping and possibly mitochondrial permeability. By means of high-resolution localization and tracking of single molecules, we have probed the current view of static $F_1F_O$ ATP synthase organization as series of dimers aligned at the edges of cristae. Our results rather suggest that subpopulations of complex V with different distribution and mobility exist in the inner membrane compartments. Under normal respiratory conditions, complex V was mainly localized in cristae, while under metabolic stress and nutrient deprivation with decreased respiration this specific spatio-temporal pattern became intermediately blurred. We suggest that in addition to modification of the metabolic setting, a shift in the ratio of oligomeric/dimeric $F_1F_O$ ATP synthase to monomeric forms is correlated with different distribution and mobility in the inner mitochondrial membrane compartments. Such dynamics would allow the simultaneous existence of ATP synthesis and ATP hydrolysis function, but spatially separated.

Supplementary data to this article can be found online at https://doi.org/10.1016/j.bbabio.2019.148091.

## Funding

This work was supported by the DFG (INST 190/167-2). K. Busch is associated with the CiM (Cells in Motion cluster, Münster).

## Author contributions

Conception and design: K.B.B., T.A., B.R.
Acquisition of data: K.Z., B.R., F.H., K.P., S.C.
Analysis software: C.P.R.
Analysis and interpretation of data: K.Z., T.A., S.C., C.P.R., B.R., K.B.B.,
Write or revise the article: K.B.B.

## Transparency document

The Transparency document associated with this article can be found, in online version.

## Declaration of competing interest

The authors do not declare any competing financial interests.

## Acknowledgments

The authors thank Wladislaw Kohl for excellent technical support.

## References

[1] M.V. Liberti, J.W. Locasale, The Warburg effect: how does it benefit cancer cells? Trends Biochem. Sci. 41 (2016) 211–218.
[2] O. Warburg, On respiratory impairment in cancer cells, Science 124 (1956) 269–270.
[3] R. Rossignol, R. Gilkerson, R. Aggeler, K. Yamagata, S.J. Remington, R.A. Capaldi, Energy substrate modulates mitochondrial structure and oxidative capacity in cancer cells, Cancer Res. 64 (2004) 985–993.
[4] G. Benard, N. Bellance, C. Jose, S. Melser, K. Nouette-Gaulain, R. Rossignol, Multi-site control and regulation of mitochondrial energy production, Biochim. Biophys. Acta 1797 (2010) 698–709.
[5] E.P. Bulthuis, M.J.W. Adjobo-Hermans, P. Willems, W.J.H. Koopman, Mitochondrial morphofunction in mammalian cells, Antioxid. Redox Signal. 30 (2019) 2066–2109.
[6] D. Dikov, J. Bereiter-Hahn, Inner membrane dynamics in mitochondria, J. Struct. Biol. 183 (2013) 455–466.
[7] M. Picard, M.J. McManus, G. Csordas, P. Varnai, G.W. Dorn 2nd, D. Williams, G. Hajnoczky, D.C. Wallace, Trans-mitochondrial coordination of cristae at regulated membrane junctions, Nat. Commun. 6 (2015) 6259.
[8] C. Frezza, S. Cipolat, O. Martins de Brito, M. Micaroni, G.V. Beznoussenko, T. Rudka, D. Bartoli, R.S. Polishuck, N.N. Danial, B. De Strooper, L. Scorrano, OPA1 controls apoptotic cristae remodeling independently from mitochondrial fusion, Cell 126 (2006) 177–189.
[9] M. Barbot, D.C. Jans, C. Schulz, N. Denkert, B. Kroppen, M. Hoppert, S. Jakobs, M. Meinecke, Mic10 oligomerizes to bend mitochondrial inner membranes at cristae junctions, Cell Metab. 21 (2015) 756–763.
[10] J.R. Friedman, A. Mourier, J. Yamada, J.M. McCaffery, J. Nunnari, MICOS coordinates with respiratory complexes and lipids to establish mitochondrial inner membrane architecture, Elife 4 (2015).
[11] F. Wollweber, K. von der Malsburg, M. van der Laan, M. contact site cristae organizing system, A central player in membrane shaping and crosstalk, Biochim. Biophys. Acta, Mol. Cell Res. 1864 (2017) 1481–1489.
[12] K.M. Davies, C. Anselmi, I. Wittig, J.D. Faraldo-Gomez, W. Kuhlbrandt, Structure of the yeast F1Fo-ATP synthase dimer and its role in shaping the mitochondrial cristae, Proc. Natl. Acad. Sci. U. S. A. 109 (2012) 13602–13607.
[13] R. Quintana-Cabrera, C. Quirin, C. Glytsou, M. Corrado, A. Urbani, A. Pellattiero, E. Calvo, J. Vazquez, J.A. Enriquez, C. Gerle, M.E. Soriano, P. Bernardi, L. Scorrano, The cristae modulator optic atrophy 1 requires mitochondrial ATP synthase oligomers to safeguard mitochondrial function, Nat. Commun. 9 (2018) 3399.
[14] K. Eydt, K.M. Davies, C. Behrendt, I. Wittig, A.S. Reichert, Cristae architecture is determined by an interplay of the MICOS complex and the F1FO ATP synthase via Mic27 and Mic10, Microb. Cell 4 (2017) 259–272.
[15] N.V. Dudkina, S. Sunderhaus, H.P. Braun, E.J. Boekema, Characterization of dimeric ATP synthase and cristae membrane ultrastructure from Saccharomyces and Polytomella mitochondria, FEBS Lett. 580 (2006) 3427–3432.
[16] R.D. Allen, C.C. Schroeder, A.K. Fok, An investigation of mitochondrial inner membranes by rapid-freeze deep-etch techniques, J. Cell Biol. 108 (1989) 2233–2240.
[17] L. Plecita-Hlavata, H. Engstova, L. Alan, T. Spacek, A. Dlaskova, K. Smolkova, J. Spackova, J. Tauber, V. Stradalova, J. Malinsky, M. Lessard, J. Bewersdorf, P. Jezek, Hypoxic HepG2 cell adaptation decreases ATP synthase dimers and ATP production in inflated cristae by mitofilin down-regulation concomitant to MICOS clustering, FASEB J. 30 (2016) 1941–1957.
[18] A. Dlaskova, H. Engstova, T. Spacek, A. Kahancova, V. Pavluch, K. Smolkova, J. Spackova, M. Bartos, L.P. Hlavata, P. Jezek, 3D super-resolution microscopy reflects mitochondrial cristae alternations and mtDNA nucleoid size and distribution, Biochim. Biophys. Acta Bioenerg. 1859 (2018) 829–844.
[19] T. Appelhans, C.P. Richter, V. Wilkens, S.T. Hess, J. Piehler, K.B. Busch, Nanoscale organization of mitochondrial microcompartments revealed by combining tracking and localization microscopy, Nano Lett. 12 (2012) 610–616.
[20] V.M. Sukhorukov, J. Bereiter-Hahn, Anomalous diffusion induced by cristae geometry in the inner mitochondrial membrane, PLoS One 4 (2009) e4604.
[21] V.M. Sukhorukov, D. Dikov, K. Busch, V. Strecker, I. Wittig, J. Bereiter-Hahn,

Determination of protein mobility in mitochondrial membranes of living cells, Biochim. Biophys. Acta 1798 (2010) 2022–2032.
[22] H. Pelicano, D.S. Martin, R.H. Xu, P. Huang, Glycolysis inhibition for anticancer treatment, Oncogene 25 (2006) 4633–4646.
[23] R. Yamaguchi, E. Janssen, G. Perkins, M. Ellisman, S. Kitada, J.C. Reed, Efficient elimination of cancer cells by deoxyglucose-ABT-263/737 combination therapy, PLoS One 6 (2011) e24102.
[24] T. Appelhans, K. Busch, Single molecule tracking and localization of mitochondrial protein complexes in live cells, Methods Mol. Biol. 1567 (2017) 273–291.
[25] A. Sergé, N. Bertaux, H. Rigneault, D. Marguet, Dynamic multiple-target tracing to probe spatiotemporal cartography of cell membranes, Nat. Methods 5 (2008) 687–694.
[26] R.C. Scaduto Jr., L.W. Grotyohann, Measurement of mitochondrial membrane potential using fluorescent rhodamine derivatives, Biophys. J. 76 (1999) 469–477.
[27] W. Pendergrass, N. Wolf, M. Poot, Efficacy of MitoTracker Green and CMXrosamine to measure changes in mitochondrial membrane potentials in living cells and tissues, Cytometry A 61 (2004) 162–169.
[28] H. Imamura, K.P. Nhat, H. Togawa, K. Saito, R. Iino, Y. Kato-Yamada, T. Nagai, H. Noji, Visualization of ATP levels inside single living cells with fluorescence resonance energy transfer-based genetically encoded indicators, Proc. Natl. Acad. Sci. U. S. A. 106 (2009) 15651–15656.
[29] T. Appelhans, F.R. Beinlich, C.P. Richter, R. Kurre, K.B. Busch, Multi-color localization microscopy of single membrane proteins in organelles of live mammalian cells, JoVE (2018) e57690.
[30] B. Muster, W. Kohl, I. Wittig, V. Strecker, F. Joos, W. Haase, J. Bereiter-Hahn, K. Busch, Respiratory chain complexes in dynamic mitochondria display a patchy distribution in life cells, PLoS One 5 (2010) e11910.
[31] M. Rosselin, J. Santo-Domingo, F. Bermont, M. Giacomello, N. Demaurex, L-OPA1 regulates mitoflash biogenesis independently from membrane fusion, EMBO Rep. 18 (2017) 451–463.
[32] M. Tokunaga, N. Imamoto, K. Sakata-Sogawa, Highly inclined thin illumination enables clear single-molecule imaging in cells, Nat. Methods 5 (2008) 159–161.
[33] E. Betzig, G.H. Patterson, R. Sougrat, O.W. Lindwasser, S. Olenych, J.S. Bonifacino, M.W. Davidson, J. Lippincott-Schwartz, H.F. Hess, Imaging intracellular fluorescent proteins at nanometer resolution, Science 313 (2006) 1642–1645.
[34] T.J. Gould, V.V. Verkhusha, S.T. Hess, Imaging biological structures with fluorescence photoactivation localization microscopy, Nat. Protoc. 4 (2009) 291–308.
[35] S.T. Hess, T.P. Girirajan, M.D. Mason, Ultra-high resolution imaging by fluorescence photoactivation localization microscopy, Biophys. J. 91 (2006) 4258–4272.
[36] S. Schmitt, F. Saathoff, L. Meissner, E.M. Schropp, J. Lichtmannegger, S. Schulz, C. Eberhagen, S. Borchard, M. Aichler, J. Adamski, N. Plesnila, S. Rothenfusser, G. Kroemer, H. Zischka, A semi-automated method for isolating functionally intact mitochondria from cultured cells and tissue biopsies, Anal. Biochem. 443 (2013) 66–74.
[37] R. Acin-Perez, P. Fernandez-Silva, M.L. Peleato, A. Perez-Martos, J.A. Enriquez, Respiratory active mitochondrial supercomplexes, Mol. Cell 32 (2008) 529–539.
[38] I. Wittig, M. Karas, H. Schagger, High resolution clear native electrophoresis for in-gel functional assays and fluorescence studies of membrane protein complexes, Mol. Cell. Proteomics 6 (2007) 1215–1225.
[39] P.E. Porporato, N. Filigheddu, J.M.B. Pedro, G. Kroemer, L. Galluzzi, Mitochondrial metabolism and cancer, Cell Res. 28 (2018) 265–280.
[40] A.S. Divakaruni, G.W. Rogers, A.N. Murphy, Measuring mitochondrial function in permeabilized cells using the seahorse XF analyzer or a clark-type oxygen electrode, Curr. Protoc. Toxicol. 60 (25 22) (2014) (21–16).
[41] S.A. Mookerjee, A.A. Gerencser, D.G. Nicholls, M.D. Brand, Quantifying intracellular rates of glycolytic and oxidative ATP production and consumption using extracellular flux measurements, J. Biol. Chem. 293 (2018) 12649–12652.
[42] M.R. Depaoli, F. Karsten, C.T. Madreiter-Sokolowski, C. Klec, B. Gottschalk, H. Bischof, E. Eroglu, M. Waldeck-Weiermair, T. Simmen, W.F. Graier, R. Malli, Real-time imaging of mitochondrial ATP dynamics reveals the metabolic setting of single cells, Cell Rep. 25 (2018) 501–512 (e503).
[43] J.D. Wikstrom, S.M. Katzman, H. Mohamed, G. Twig, S.A. Graf, E. Heart, A.J. Molina, B.E. Corkey, L.M. de Vargas, N.N. Danial, S. Collins, O.S. Shirihai, beta-Cell mitochondria exhibit membrane potential heterogeneity that can be altered by stimulatory or toxic fuel levels, Diabetes 56 (2007) 2569–2578.
[44] G.J. Grover, J. Malm, Pharmacological profile of the selective mitochondrial F1F0 ATP hydrolase inhibitor BMS-199264 in myocardial ischemia, Cardiovasc. Ther. 26 (2008) 287–296.
[45] D.A. Patten, J. Wong, M. Khacho, V. Soubannier, R.J. Mailloux, K. Pilon-Larose, J.G. MacLaurin, D.S. Park, H.M. McBride, L. Trinkle-Mulcahy, M.E. Harper, M. Germain, R.S. Slack, OPA1-dependent cristae modulation is essential for cellular adaptation to metabolic demand, EMBO J. 33 (2014) 2676–2691.
[46] M. Strauss, G. Hofhaus, R.R. Schroder, W. Kuhlbrandt, Dimer ribbons of ATP synthase shape the inner mitochondrial membrane, EMBO J. 27 (2008) 1154–1160.
[47] T. Appelhans, K.B. Busch, Dynamic imaging of mitochondrial membrane proteins in specific sub-organelle membrane locations, Biophys. Rev. 9 (2017) 345–352.
[48] H. Shen, L.J. Tauzin, R. Baiyasi, W. Wang, N. Moringo, B. Shuang, C.F. Landes, Single Particle Tracking: From Theory to Biophysical Applications, Chem. Rev. 117 (2017) 7331–7376.
[49] V. Wilkens, W. Kohl, K. Busch, Restricted diffusion of OXPHOS complexes in dynamic mitochondria delays their exchange between cristae and engenders a transitory mosaic distribution, J. Cell Sci. 126 (2013) 103–116.
[51] S. Stoldt, D. Wenzel, K. Kehrein, D. Riedel, M. Ott, S. Jakobs, Spatial orchestration of mitochondrial translation and OXPHOS complex assembly, Nat. Cell Biol. 20 (2018) 528–534.
[52] K.M. Davies, M. Strauss, B. Daum, J.H. Kief, H.D. Osiewacz, A. Rycovska, V. Zickermann, W. Kuhlbrandt, Macromolecular organization of ATP synthase and complex I in whole mitochondria, Proc. Natl. Acad. Sci. U. S. A. 108 (2011) 14121–14126.
[53] K. Wagner, P. Rehling, L.K. Sanjuan Szklarz, R.D. Taylor, N. Pfanner, M. van der Laan, Mitochondrial F1Fo-ATP synthase: the small subunits e and g associate with monomeric complexes to trigger dimerization, J. Mol. Biol. 392 (2009) 855–861.
[54] I. Arnold, K. Pfeiffer, W. Neupert, R.A. Stuart, H. Schagger, Yeast mitochondrial F1F0-ATP synthase exists as a dimer: identification of three dimer-specific subunits, EMBO J. 17 (1998) 7170–7178.
[55] J.R. Gledhill, M.G. Montgomery, A.G. Leslie, J.E. Walker, How the regulatory protein, IF(1), inhibits F(1)-ATPase from bovine mitochondria, Proc. Natl. Acad. Sci. U. S. A. 104 (2007) 15671–15676.
[56] M. Campanella, E. Casswell, S. Chong, Z. Farah, M.R. Wieckowski, A.Y. Abramov, A. Tinker, M.R. Duchen, Regulation of mitochondrial structure and function by the F1Fo-ATPase inhibitor protein, IF1, Cell Metab. 8 (2008) 13–25.
[57] P.D. Gavin, M. Prescott, R.J. Devenish, F1F0-ATP synthase complex interactions in vivo can occur in the absence of the dimer specific subunit e, J. Bioenerg. Biomembr. 37 (2005) 55–66.
[58] I. Wittig, J. Velours, R. Stuart, H. Schagger, Characterization of domain interfaces in monomeric and dimeric ATP synthase, Mol. Cell. Proteomics 7 (2008) 995–1004.
[59] L. Sanchez-Cenizo, L. Formentini, M. Aldea, A.D. Ortega, P. Garcia-Huerta, M. Sanchez-Arago, J.M. Cuezva, Up-regulation of the ATPase inhibitory factor 1 (IF1) of the mitochondrial H+-ATP synthase in human tumors mediates the metabolic shift of cancer cells to a Warburg phenotype, J. Biol. Chem. 285 (2010) 25308–25313.
[60] M. Pelosse, C. Cottet-Rousselle, C.M. Bidan, A. Dupont, K. Gupta, I. Berger, U. Schlattner, Synthetic energy sensor AMPfret deciphers adenylate-dependent AMPK activation mechanism, Nat. Commun. 10 (2019) 1038.
[61] J. Garcia-Bermudez, J.M. Cuezva, The ATPase inhibitory factor 1 (IF1): a master regulator of energy metabolism and of cell survival, Biochim. Biophys. Acta 1857 (2016) 1167–1182.
[62] F. Vogel, C. Bornhovd, W. Neupert, A.S. Reichert, Dynamic subcompartmentalization of the mitochondrial inner membrane, J. Cell Biol. 175 (2006) 237–247.
[63] A. Dlaskova, T. Spacek, H. Engstova, J. Spackova, A. Schrofel, B. Holendova, K. Smolkova, L. Plecita-Hlavata, P. Jezek, Mitochondrial cristae narrowing upon higher 2-oxoglutarate load, Biochim. Biophys. Acta Bioenerg. 1860 (2019) 659–678.
[64] J. Habersetzer, I. Larrieu, M. Priault, B. Salin, R. Rossignol, D. Brethes, P. Paumard, Human F1F0 ATP synthase, mitochondrial ultrastructure and OXPHOS impairment: a (super-)complex matter? PLoS One 8 (2013) e75429.
[65] P. Paumard, J. Vaillier, B. Coulary, J. Schaeffer, V. Soubannier, D.M. Mueller, D. Brethes, J.P. di Rago, J. Velours, The ATP synthase is involved in generating mitochondrial cristae morphology, EMBO J. 21 (2002) 221–230.
[66] N.V. Dudkina, G.T. Oostergetel, D. Lewejohann, H.P. Braun, E.J. Boekema, Row-like organization of ATP synthase in intact mitochondria determined by cryo-electron tomography, Biochim. Biophys. Acta 1797 (2010) 272–277.
[67] P.D. Gavin, M. Prescott, S.E. Luff, R.J. Devenish, Cross-linking ATP synthase complexes in vivo eliminates mitochondrial cristae, J. Cell Sci. 117 (2004) 2333–2343.
[68] N.V. Dudkina, J. Heinemeyer, W. Keegstra, E.J. Boekema, H.P. Braun, Structure of dimeric ATP synthase from mitochondria: an angular association of monomers induces the strong curvature of the inner membrane, FEBS Lett. 579 (2005) 5769–5772.
[69] T. Brandt, A. Mourier, L.S. Tain, L. Partridge, N.G. Larsson, W. Kuhlbrandt, Changes of mitochondrial ultrastructure and function during ageing in mice and Drosophila, Elife 6 (2017).
[70] B. Daum, A. Walter, A. Horst, H.D. Osiewacz, W. Kuhlbrandt, Age-dependent dissociation of ATP synthase dimers and loss of inner-membrane cristae in mitochondria, Proc. Natl. Acad. Sci. U. S. A. 110 (2013) 15301–15306.
[71] E. Koltai, N. Hart, A.W. Taylor, S. Goto, J.K. Ngo, K.J. Davies, Z. Radak, Age-associated declines in mitochondrial biogenesis and protein quality control factors are minimized by exercise training, Am. J. Phys. Regul. Integr. Comp. Phys. 303 (2012) R127–R134.
[72] R. Acin-Perez, J.A. Enriquez, The function of the respiratory supercomplexes: the plasticity model, Biochim. Biophys. Acta 1837 (2014) 444–450.
[73] S. Cogliati, C. Frezza, M.E. Soriano, T. Varanita, R. Quintana-Cabrera, M. Corrado, S. Cipolat, V. Costa, A. Casarin, L.C. Gomes, E. Perales-Clemente, L. Salviati, P. Fernandez-Silva, J.A. Enriquez, L. Scorrano, Mitochondrial cristae shape determines respiratory chain supercomplexes assembly and respiratory efficiency, Cell 155 (2013) 160–171.